Mitochondrial fission controls astrocyte morphogenesis and organization in the cortex

Maria Pia Rodriguez Salazar[1], Sprihaa Kolanukuduru1[1,2], Valentina Ramirez[1,3], Boyu Lyu[4], Gabrielle Sejourne[1], Hiromi Sesaki[5], Guoqiang Yu[6,7], Cagla Eroglu[1,8,9,10*]

1 The Department of Cell Biology, Duke University Medical Center, Durham, NC, USA

2 The Department of Psychology and Neuroscience, University of North Carolina at Chapel Hill, Chapel Hill, NC, USA

3 The Department of Psychology and Neuroscience, Duke University, Durham, NC, USA

4 Bradley Department of Electrical and Computer Engineering, Virginia Polytechnic Institute and State University, Arlington, VA, USA

5 Department of Cell Biology, John Hopkins University School of Medicine, Baltimore, MD

6 Department of Automation, Tsinghua University, Beijing 100084, China

7 IDG/McGovern Institute for Brain Research, Tsinghua University, Beijing 100084, China

8 Aligning Science Across Parkinson's (ASAP) Collaborative Research Network, Chevy Chase, MD

9 The Department of Neurobiology, Duke University Medical Center, Durham, NC, USA

10 Howard Hughes Medical Institute, Duke University Medical Center, Durham, NC, USA

*Corresponding author: Cagla Eroglu: cagla.eroglu@duke.edu

Summary:

During cortical astrocyte morphogenesis, mitochondria decrease in size to populate distal astrocyte processes. Drp1-mediated mitochondrial fission is necessary for peripheral astrocyte process formation. Astrocyte-specific Drp1 loss induces astrocyte reactivity, disrupts cortical astrocyte organization, and dysregulates gap-junction protein Connexin 43 abundance.

ABSTRACT

Dysfunctional mitochondrial dynamics are a hallmark of devastating neurodevelopmental disorders such as childhood refractory epilepsy. However, the role of glial mitochondria in proper brain development is not well understood. We show that astrocyte mitochondria undergo extensive fission while populating astrocyte distal branches during postnatal cortical development. Loss of mitochondrial fission regulator, Dynamin-related protein 1 (Drp1), decreases mitochondrial localization to distal astrocyte processes, and this mitochondrial mislocalization reduces astrocyte morphological complexity. Functionally, astrocyte-specific conditional deletion of Drp1 induces astrocyte reactivity and disrupts astrocyte organization in the cortex. These morphological and organizational deficits are accompanied by loss of astrocytic gap junction protein Connexin 43. These findings uncover a crucial role for mitochondrial fission in coordinating astrocytic morphogenesis and organization, revealing the regulation of astrocytic mitochondria dynamics as a critical step in neurodevelopment.

INTRODUCTION

Mitochondria are dynamic organelles that move, divide, and fuse in response to changing cellular states (Friedman and Nunnari, 2014; Youle and van der Bliek, 2012). Localized functions of mitochondria within cells are governed by fusion, fission, and trafficking processes, collectively referred to as mitochondrial dynamics (Ni et al., 2015). Mitochondrial dynamics are particularly important for the function and development of highly compartmentalized cells such as neurons, where mitochondria within distal compartments perform key functions including ion buffering, energy production, and local protein translation (Billups and Forsythe, 2002; López-Doménech and Kittler, 2023; Rangaraju et al., 2019). Furthermore, distal mitochondria regulate cellular morphology of neurons through focalized ATP generation for actin polymerization at growth cones, and disruptions in mitochondrial dynamics result in stunted neurite growth (Courchet et al., 2013; Smith and Gallo, 2018; Steketee et al., 2012). Indeed, mutations in the genes that control the mitochondrial dynamics' machinery cause severe neurodevelopmental disorders, such as forms of childhood refractory epilepsy (Abati et al., 2022; Vanstone et al., 2016).

Despite the clear importance of mitochondrial dynamics in brain development, the role of this organelle in non-neuronal brain cells is less well understood. In particular, astrocytes are the most abundant glial cells in the brain and have highly ramified processes that make up more than half of the brain parenchyma by infiltrating the neuropil. These fine astrocyte processes interact with synapses, vasculature, and other glia (Allen and Lyons, 2018) where they regulate synapse formation, neurotransmitter and ion buffering, and maintain the blood-brain barrier (Alvarez et al., 2013; Chung et al., 2015). Intriguingly, astrocyte peripheral processes are loaded with mitochondria at higher densities than the surrounding neuropil (Lovatt et al., 2007), and their mitochondria are recruited to perisynapses in response to neuronal activity (Stephen et al., 2015), linking astrocyte mitochondrial dynamics and synapse function. Indeed, mature astrocyte mitochondria localize to functional microdomains in their arbors, where mitochondria regulate distal calcium dynamics to provide metabolic support in response to neuronal activity (Agarwal et al., 2017). Furthermore, recent work established that immature astrocytes have a high oxidative capacity and require mitochondrial biogenesis for proper morphogenesis and synapse formation (Zehnder et al., 2021). However, the role of mitochondrial dynamics in astrocyte development is unknown.

Beyond their morphological complexity, another way in which astrocytes regulate brain homeostasis is by tiling the entire brain parenchyma in evenly dispersed, non-overlapping domains. This organization enables astrocytes to form an extensive network that facilitates long-distance communication via gap junction-coupling between the distal processes of neighboring astrocytes (Bushong et al., 2002; Giaume et al., 2010). Tiling is absent in immature astrocytes, becomes established as astrocytes mature, and is regulated by the same machinery that ensures proper gap junction coupling via Connexin 43 (Cx43) (Baldwin et al., 2021). Cx43 is the most abundant gap junction protein in the brain and is almost exclusively expressed in astrocytes (Rash et al., 2001). Beyond its gap junction roles, Cx43 has cell-adhesion functions that drive astrocyte morphogenesis and migration (Kameritsch et al., 2012; Lagos-Cabré et al., 2019). Importantly, both tiling and gap junction-coupling are disrupted in many forms of brain injury and disease such as epilepsy and traumatic brain injury, indicating the importance of the proper establishment of astrocyte networks in brain homeostasis (Cheung et al., 2023; Clasadonte et al., 2017; Hösli et al., 2022; Oberheim et al., 2008).

Here, we investigated the role of mitochondrial dynamics in astrocyte morphogenesis, development, and function. We found that astrocyte mitochondria robustly increase in number and decrease in size to populate distal astrocyte processes during postnatal development, linking mitochondrial fission, to astrocyte morphogenesis. Dynamin-related protein 1 (Drp1), encoded by the gene *Dnm1l,* is a highly conserved GTPase that controls mitochondrial fission (Chang and Blackstone, 2010; Fonseca et al., 2019; Smirnova et al., 2001). Upon mitochondrial division, Drp1 recruited to the outer mitochondrial membrane to perform GTP hydrolysis-driven scission (Losón et al., 2013; Smirnova et al., 2001; Uo et al., 2009). Complete loss of Drp1 is embryonically lethal in mice (Wakabayashi et al., 2009b) and mutations in human *DNM1L* are linked to aggressive forms of developmental delay and childhood refractory epilepsy (Fahrner et al., 2016; Liu et al., 2021). Despite the causal link between Drp1 function and proper brain development, the role of Drp1 in astrocyte morphogenesis and development is unknown.

RESULTS

Mitochondria increase in number and decrease in size during cortical astrocyte morphogenesis

In mature astrocytes, mitochondria occupy the entirety of the astrocyte arbor (Lovatt et al., 2007) and this mitochondrial dispersion is remodeled in response to injury or disease (Gollihue and Norris, 2020; Motori et al., 2013). However, it is not well understood how the mitochondrial network is established and modified in developing astrocytes. Namely, how do mitochondrial transport, fission, or fusion dynamics orchestrate the distribution of astrocytic mitochondria during morphogenesis? To address this question, we first investigated how the mitochondrial network transforms during astrocyte maturation to populate the arbors. To do so, we used Postnatal Astrocyte Labeling by Electroporation (PALE) (Stogsdill et al., 2017) to fluorescently label sparse populations of astrocytes in the developing mouse V1 visual cortex. We used Mito-EGFP floxed mice (Agarwal et al., 2017), in which EGFP is targeted to the inner mitochondrial membrane protein cytochrome c oxidase, to label all mitochondria in Cre-expressing cells. We electroporated two plasmids into the ventricles of P0 mice— a pCAG-Cre plasmid to turn on the mitochondrial GFP and an mCherry-CAAX plasmid to label astrocyte membranes. Then using confocal microscopy, we imaged and analyzed astrocytes from layers 2/3, 4, and 5 of the developing visual cortex. This approach allowed us to visualize and quantify astrocyte morphology and their mitochondrial content throughout postnatal cortical development using confocal microscopy and morphometric analyses (Fig. 1A).

We focused our studies on the first 3 weeks of postnatal astrocyte development (P4, P7, P14, P21, Fig. 1B), because cortical astrocytes become morphological mature during this period (Clavreul et al., 2019; Stogsdill et al., 2017). As expected, astrocytes undergo robust growth and elaboration, increasing their overall cell volume approximately 20-fold between P4 and P21 (Fig. 1C). Concurrently, we found that total astrocyte mitochondrial volume per cell increased 5-fold between P4 and P14 and then remained constant between P14 and P21 (Fig. 1D). We next quantified total mitochondrial volume per cell normalized to astrocyte cell volume, hereafter referred to as total mitochondrial occupancy. We found total mitochondrial occupancy decreased during development due to the robust increase in astrocyte cell volume (Fig. 1E). Importantly, astrocyte mitochondria increased in number and decreased in size on average during these first two postnatal weeks (Fig.

1F-G), indicating mitochondria division (fission) occurs concurrently with astrocyte morphogenesis.

Mitochondria occupy fine astrocyte processes concurrently with morphogenesis *in vitro*

The recruitment of mitochondria to the distal edge of developing cell processes in other compartmentalized cells is required for cytoskeletal remodeling and branch outgrowth (Cunniff et al., 2016; Li et al., 2004; López-Doménech et al., 2016; Smith and Gallo, 2018; Steketee et al., 2012). However, the spatiotemporal distribution of mitochondria during astrocyte arborization and whether astrocyte mitochondria are present at the tips of their developing peripheral processes is not known. The highly complex morphology of astrocytes *in vivo* obstructs our ability to track and analyze individual astrocyte processes and their mitochondria. Therefore, we investigated how mitochondria are distributed throughout the astrocyte arbor during morphological growth using an *in vitro* astrocyte-neuron co-culture system. Astrocytes cultured on top of neurons gain a complex morphology compared to astrocytes cultured alone or with non-neuronal cells (Stogsdill et al., 2017). Thus, we used astrocyte-neuron co-cultures to stimulate astrocyte ramification and track how mitochondrial number, size, and distribution change during process elaboration. We isolated and transfected primary cortical rat astrocytes with cytosolic GFP and MitoDsRed constructs to label astrocytes and their mitochondria, respectively. Transfected astrocytes were then plated onto rat cortical neuron monolayers for 4, 12, 24, and 48 hours (Fig. 2A-B).

We developed a Matlab-based image analysis program, Seg_Astro (https://github.com/Eroglu-Lab/seg_cul_astro_app/tree/main) to quantify branch number, mitochondrial number, and mitochondrial size across astrocyte arbors. Seg_Astro uses branch width and branchpoints to determine the astrocyte branch hierarchy and assign four branch types: 1) soma and primary processes, 2) secondary processes, 3) fine processes, and 4) the terminal tips of processes (Fig. 2C). Seg_Astro then bins mitochondria into these 4 types of branches and outputs branch number, mitochondrial number, and mitochondrial size per branch type. We excluded mitochondrial measurements from the soma and primary branches of astrocytes as mitochondria form dense network in these compartments that cannot be distinguished as discrete mitochondria for number and size quantification.

154 Seg_astro quantification showed a significant increase across all astrocyte branch types (primary,
155 secondary, fine, and terminal) between 4hr and 48hr in culture. Strikingly, astrocyte fine branches
156 had the largest increase in number, quadrupling from 4 to 48 hours in culture (Fig 2D). Intriguingly,
157 mitochondria were present across all astrocyte branch types including fine and terminal, as early
158 as 4 hours and through 48 hours in co-culture (Fig. 2B Inset and 2E). These results show that
159 mitochondria occupy distal processes during astrocyte branch development in vitro and suggest
160 that mitochondrial recruitment to these distal processes may be required for sustained growth of
161 astrocyte arbors.

162 Our analyses also revealed astrocyte mitochondria numbers increased across all branch types
163 throughout time in culture, with fine branches housing the largest increase in number of
164 mitochondria, 3-fold, by 48 hours in culture (Fig. 2E). While mitochondrial numbers increased,
165 average mitochondrial size decreased across all astrocyte branch types throughout time in culture
166 *except* in fine processes which housed small mitochondria throughout morphogenesis (Fig. 2F).
167 This result suggested that mitochondrial fission may be required for mitochondrial recruitment to
168 the growing fine/distal processes as there may be a maximum size threshold for mitochondria to
169 occupy fine astrocyte branches. These data echo and expand upon our *in vivo* findings and
170 implicate a role for mitochondrial division in distal astrocyte process morphogenesis.

171

172 **Drp1-induced mitochondrial fission is required for distal astrocyte process formation and**
173 **mitochondrial localization *in vitro***

174 Because cortical astrocyte morphogenesis occurred concurrently with extensive mitochondrial
175 fragmentation *in vivo* and *in vitro*, we next investigated the role of mitochondrial fission in
176 astrocyte development. We knocked down Drp1, the key GTPase regulator of mitochondrial
177 fission (Smirnova et al., 2001) (Fig. 3A-B), in astrocytes using a small hairpin RNA (shRNA)
178 targeting both the rat and mouse mRNAs (Sup. Fig. 2A-B) and assessed how it affected astrocyte
179 morphological complexity in co-culture with neurons. We co-transfected GFP-expressing shDrp1
180 or a scrambled control shRNA (shControl) and MitoDsRed into astrocytes and co-cultured them
181 on neurons for 48 hours. We used Seg_Astro to quantify mitochondrial and branch number per
182 branch type in shControl and shDrp1 astrocytes (Fig. 3C). We found that Drp1 knockdown
183 significantly decreased mitochondria numbers in secondary, fine, and terminal astrocyte processes

compared to control. The largest decrease in mitochondria numbers was in fine/distal branches, to less than 40% of shControl (Fig. 3D). Concurrently, shDrp1 astrocytes had a significant decrease of exclusively fine and terminal astrocyte process number compared to shControl. shDrp1 did not affect primary or secondary branch numbers (Fig. 3E). These data demonstrate that Drp1-induced mitochondrial fission is specifically required for fine and terminal astrocyte process formation, likely through regulation mitochondrial size and recruitment to these fine processes.

To determine if Drp1 GTPase activity-driven scission is necessary for its role in astrocyte distal process morphogenesis, we implemented human Drp1 constructs that are resistant to shDrp1 (Sup. Fig. 2A); wild-type human Drp1 (hDrp1) and GTPase-dead point mutant human Drp1 (hDrp1-K38E) (Fig. 3B) (König et al., 2021). The co-transfection of shDrp1 with hDrp1 rescued astrocyte distal process formation compared to shDrp1 alone, whereas the GTPase-dead counterpart could not (Fig. 3F-J). Together these data reveal that Drp1-mediated mitochondrial fission is necessary for the formation of fine/distal astrocyte branches *in vitro*. These data also suggest that mitochondrial recruitment to distal processes is facilitated by mitochondrial fission, and this recruitment is required for astrocyte fine branch formation and/or stabilization during astrocyte morphological growth.

Drp1 controls mitochondrial occupancy and distal astrocyte process morphogenesis *in vivo*

Because Drp1 is required for distal astrocyte branch formation *in vitro,* we next tested whether Drp1-mediated mitochondrial fission (Fig. 4A) would play a similar role in cortical astrocyte morphogenesis *in vivo.* To address this question, we used PALE to electroporate plasmids with shDrp1 or shControl into the ventricle of P0 Mito-EGFP floxed mice. These plasmids also express a membrane-tagged mCherry reporter, which we used to quantify astrocyte morphology. They were delivered together with a Cre-expressing plasmid, which drives Mito-EGFP expression to determine mitochondrial morphology at P21. We used Imaris to render 3D surfaces of astrocytes and their mitochondria and measure overall astrocyte territory size, the volume of distal neuropil-infiltrating astrocyte processes (Neuropil Infiltration Volume; NIV), and total mitochondrial volume in the whole astrocyte or the distal processes. Using these methods, we investigated how loss of Drp1 in cortical astrocytes *in vivo* impacted astrocyte territory size, distal process formation, and mitochondrial localization within the astrocyte arbors.

214 Interestingly, shDrp1 had no effect on astrocyte territory size or total mitochondrial content per
215 cell (Fig. 4B, Sup. Fig. 2A-B). However, Drp1 knockdown significantly decreased mitochondrial
216 localization to dital astrocyte regions, which was accompanied by a significant decrease in the
217 volume of distal neuropil-infiltrating astrocyte processes (Fig. 4C-D). These results suggest that
218 mitochondrial fission controls mitochondrial recruitment to distal/perisynaptic astrocyte processes
219 which is required for proper neuropil infiltration by astrocytes *in vivo*.

220 To determine if distal astrocyte process formation was specifically controlled by Drp1-induced
221 mitochondrial fission or a byproduct of modifying mitochondrial dynamics in general, we tested
222 how disrupting mitochondrial fusion by knocking down Mitofusin1 or inhibiting mitochondrial
223 transport by knocking down Miro1, modified astrocyte morphogenesis and mitochondrial
224 occupancy. Mitofusin1 (Mfn1) is a GTPase on the outer membrane of mitochondria that facilitates
225 fusion (Chen et al., 2003) (Fig. 4E). Miro1 is a GTPase adaptor that tethers the outer mitochondrial
226 membrane to cytoskeletal motors for mitochondrial transport (Fransson et al., 2006) (Fig. 4I). We
227 used PALE to electroporate shMfn1 or shMiro1 constructs (Sup. Fig. 1C-E). Interestingly,
228 silencing Mfn1 caused a reduction in astrocyte territory size (Fig. 4F) but did not alter
229 mitochondrial occupancy or the volume of distal neuropil-infiltrating processes (Fig. 4G-H, Sup.
230 Fig. 2A, C), indicating mitochondrial fusion may play a role in astrocyte territory outgrowth
231 independently of distal process complexity. Miro1 knockdown did not impact astrocyte
232 morphology or total mitochondrial content (Fig. 4J-K, Sup. Fig. 2A, D) but caused an increase in
233 the volume of mitochondria localized at the distal astrocyte processes (Fig. 4L), suggesting Miro1-
234 mediated mitochondrial trafficking may regulate retrograde mitochondrial transport in developing
235 astrocytes. Taken together, we found that mitochondrial dynamics are key regulators of astrocyte
236 morphology, likely through the control of mitochondrial localization to nascent processes. Our
237 findings show that astrocyte territory growth (large primary/secondary processes) does not require
238 Drp1 function. However, Drp1-induced mitochondrial fission, but not mitochondrial fusion or
239 transport, is necessary for the formation of distal neuropil-infiltrating astrocyte processes *in vivo.*

240

241 **Drp1 is required for astrocyte organization during postnatal cortical development**

242 During our PALE studies investigating the role of Drp1 in cortical astrocyte morphogenesis, we
243 observed an unusual clustering phenotype in shDrp1-transfected astrocytes compared to shControl

244 at P21 (Fig. 5A). PALE time course experiments from P7-P21 revealed that shDrp1 astrocytes
245 clustered as early as P7, and the clustering effect was cumulative across timepoints, reaching a
246 nearly 4-fold increase in cluster area compared to control by P21 (Fig. 5B). To determine if this
247 phenotype was due to a prolonged or exuberant astrocyte proliferation, we used Click-IT EdU
248 chemistry to label proliferating cells in the cortex of PALE mice. shControl and shDrp1 plasmids
249 were electroporated at P0, then EdU was injected intraperitoneally every two days from P3 to P13
250 and brains were collected 15 hours after EdU injection from P4 through P14 (Sup Fig. 3A). We
251 did not find any evidence of increased or prolonged cell proliferation in shDrp1 transfected
252 astrocytes compared to control (Sup. Fig. 3B, C), indicating astrocyte clustering in shDrp1-
253 transfected astrocytes is not caused by over proliferation. These shDrp1 astrocyte clusters
254 remained into adulthood (in 2 and 6-month-old mice, Sup. Fig. 3D, E), demonstrating astrocyte
255 clustering due to Drp1 loss is not a transient developmental phenomenon that resolves after
256 maturation.

257 Cortical astrocytes organize themselves into a network of evenly dispersed, non-overlapping
258 domains, which is critical for proper brain function (Bushong et al., 2004). Because early postnatal
259 loss of Drp1 led to cortical astrocyte clustering, we next sought to understand whether these
260 astrocyte clusters displayed disrupted astrocyte organization. To do so, we measured the nearest
261 neighbor distance between Sox9+ astrocyte nuclei to investigate whether shDrp1 astrocyte clusters
262 consisted of adjacent astrocytes that maintained their evenly dispersed astrocyte organization
263 (equidistant nuclei), or disorganized astrocytes with inconsistent nuclei distances (Fig. 5C). First,
264 we found that Drp1 knockdown clusters contained ~4 nuclei on average compared to control
265 astrocytes which only contain 1 nucleus (Fig. 5D), confirming that shDrp1-transfected astrocyte
266 clusters comprised multiple astrocytes. Importantly, shDrp1 astrocyte clusters had a 3-fold
267 decrease in nearest neighbor distance compared to control astrocytes (Fig. 5E), indicating a
268 disorganization among cortical astrocytes when Drp1 is knocked down. These data show that loss
269 of Drp1 impairs the astrocyte organization in the cortex by inducing clustering, suggesting Drp1
270 may play a role in the establishment of astrocyte tiling during development. Taken together these
271 data demonstrate that Drp1-induced mitochondrial fission promotes both astrocyte morphogenesis
272 and organization during postnatal development in the mouse cortex.

273 Astrocyte organization in the cortex is mechanistically linked to the formation of a gap junction-
274 coupled astrocyte network (Baldwin et al., 2021). In particular, proper expression and localization

275 of Connexin 43 (Cx43) , the most abundant astrocytic gap junction protein (Dermietzel et al.,
276 1991), is required for the establishment of non-overlapping astrocyte territories (Baldwin et al.,
277 2021; Lagos-Cabré et al., 2019). Because we observed astrocyte disorganization and clustering in
278 PALE shDrp1 astrocytes, we next wondered if loss of Drp1 caused these changes via disruption of
279 gap junctions. To test this possibility, we quantified Cx43 via immunohistochemistry within
280 shDrp1 and shControl PALE astrocytes. Strikingly, shDrp1 astrocytes had a 5-fold decrease in
281 Cx43 with visible "holes" of Cx43 staining coinciding with the shDrp1 astrocyte clusters (Fig. 5F-
282 G). These data reveal that Drp1 knockdown results in a profound reduction of Cx43 protein
283 expression in astrocytes. Importantly, this effect of shDrp1 is Cx43-specific as we did not observe
284 a change in the levels of Cx30, another gap junction protein which is also expressed by astrocytes
285 (Sup. Fig. 3F). These results also suggest that Drp1-mediated Cx43 expression and/or localization
286 may be responsible for the observed clustering phenotype of Drp1 knockdown astrocytes.

287

288 **Astrocyte-specific Drp1 knock out induces astrocyte reactivity**

289 To understand the impact of Drp1 loss in all astrocytes during cortical development, we utilized a
290 conditional (floxed) allele of mouse Drp1 (Wakabayashi et al., 2009a) which we crossed with the
291 tamoxifen-inducible astrocytic Cre-driver mouse Aldh1l1-CreERT2 (Srinivasan et al., 2016). A
292 tdTomato-floxed reporter (Ai14) was also used to identify cells expressing Cre (Fig. 6A). To delete
293 Drp1 from developing astrocytes, tamoxifen was injected into the milk spot of pups at P1, P2, and
294 P3 and mice were collected for analyses at P21 (Fig. 6A). This approach resulted in a significant
295 reduction of Drp1 protein in Drp1 conditional knock-out (cKO) astrocytes compared to wild-type
296 control (cWT) by immunoblotting of isolated cortical astrocytes (Fig. 6B-C). Further, we found
297 Drp1 protein reduced within Cre-positive (tdTomato^{+}) astrocytes across all cortical layers by
298 immunohistochemistry, with an overall significant decrease in V1 cortex in Drp1 cKO astrocytes
299 compared to control (Sup. Fig. 4A-C). These results show that Aldh1L1-CreERT2 driver along
300 with daily tamoxifen injections between P1-P3 can be used to significantly reduce astrocytic Drp1
301 expression in mice *in vivo*.

302 Because we found that shDrp1 decreased astrocyte distal process formation and caused astrocyte
303 clustering in our sparse PALE manipulation model, we wondered how global loss of Drp1 in
304 astrocytes via conditional deletion would affect astrocyte development and cortical homeostasis.

305 We found an overall decrease in astrocyte density in the cortex by tdTomato$^+$ soma count that was
306 primarily driven by decreases in L1 and L6 astrocytes in Drp1 cKO animals compared to control
307 (Fig. 6D-E). The decrease in astrocyte density did not impact overall cortical thickness (Sup. Fig.
308 4D). Next, we quantified tdTomato$^+$ signal by immunohistochemistry as a proxy for astrocyte
309 coverage and found that loss of Drp1 in cKO astrocytes significantly decreased their process
310 coverage across the cortex compared to cWT, with the greatest coverage loss found in L5 and L6
311 astrocytes (Fig. 6F). Given that our astrocyte coverage analysis was normalized by astrocyte
312 density, these data suggest this significant reduction in cortical astrocyte coverage is driven by the
313 loss of astrocyte processes formation in Drp1 cKO.

314 Astrocytes modify their morphology and coverage of the cortex under disease and injury
315 conditions (Fiebig et al., 2019; Oberheim et al., 2008). Furthermore, mature cortical astrocytes
316 express low GFAP protein under homeostatic conditions but increase their GFAP expression upon
317 entering a reactive state (Middeldorp and Hol, 2011). Because we found morphology and coverage
318 abnormalities in astrocyte-specific Drp1 cKO mice, we next tested whether the astrocytes in these
319 brains became reactive. To do so, we performed immunohistochemistry for GFAP in Drp1 cKO
320 and cWT cortices, and quantified changes in their GFAP density and coverage (Fig. 6D). We found
321 that Drp1 cKO mice had a significant increase in their cortical GFAP expression, as quantified by
322 their density and coverage, predominantly in the mid layers (L2/3, L4, and L5) compared to control
323 (Fig. 6G-H). In agreement, isolated astrocytes from Drp1 cKO mice showed increased expression
324 of GFAP and vimentin mRNA, which are linked to astrocyte reactivity (Sup. Fig. 4E-F). These
325 findings indicate a disruption in astrocyte homeostasis and suggest that conditional loss of Drp1
326 in astrocytes induces cortical astrocyte reactivity *in vivo*.

327

328 **Astrocytic Drp1 loss dysregulates Connexin 43 expression *in vivo***

329 To determine if conditional deletion of Drp1 in cortical astrocytes disrupted astrocyte organization
330 as we previously observed in our sparse PALE knockdown model (Fig. 5), we quantified both
331 nearest neighbor and multiple neighbor distances between tdTomato$^+$ somas in the cortices of cKO
332 and cWT mice (Fig. 7A). We found that in Drp1 cKO mice, astrocytes displayed significant
333 decreases in nearest neighbor distance (Fig. 7B). Further, quantification of distances between
334 multiple astrocyte neighbors revealed that Drp1 cKO astrocytes have a greater variability in

335 distances to their neighbors compared to cWT astrocytes (Fig. 7C), indicating Drp1 cKO astrocytes
336 have an unevenly dispersed distribution of astrocyte somas compared to cWT. These data identify
337 a disorganization in cortical astrocytes in the absence of Drp1. Taken together, these results are in
338 line with our findings using shRNA constructs and PALE (Fig. 5) and show that loss of Drp1 in
339 developing astrocytes disrupts cortical astrocyte organization *in vivo*.

340 Given the robust disruption to astrocyte organization in Drp1 cKO mice, we next tested how Cx43
341 expression was impacted in Drp1 cKO astrocytes compared to cWT. To do so, we stained for Cx43
342 in the cortex and found that Drp1 cKO astrocytes displayed a heterogeneous and uneven
343 expression of Cx43, with some astrocytes apparently expressing almost no Cx43 while others
344 expressed wild-type or higher levels of the protein compared to the more even distribution of Cx43
345 in cWT cortices (Fig. 7D). Indeed, quantification of Cx43 signal showed that while there was no
346 change in average Cx43 expression between genotypes (Fig. 7E), there was significant increase in
347 the variance of Cx43 expression in Drp1 cKO astrocytes compared to cWT (Fig. 7F). We
348 quantified this heterogeneity by comparing the cumulative distribution and histogram of Cx43
349 expression per astrocyte and found that Drp1 cKO astrocytes had a significantly altered
350 distribution of Cx43 expression (Fig. 7G). This heterogeneous expression of cortical Cx43 protein
351 *in situ* led us to investigate how Cx43 mRNA and protein expression may be disrupted in
352 astrocytes. To do so, we immunopurified astrocytes from the cortex and measured mRNA and
353 protein levels of Cx43. Cx43 mRNA levels were unchanged in Drp1 cKO isolated astrocytes
354 compared to cWT (Fig. 7H). Interestingly, immunoblotting for Cx43 in isolated astrocytes
355 demonstrated a robust decrease of Cx43 full-length (FL) protein as well as its internally translated
356 smaller isoforms in Drp1 cKO astrocytes compared to cWT (Fig. 7I). Importantly, the trafficking
357 of Cx43-FL to the cell membrane to carry out its gap junction and cell-adhesion functions is
358 regulated by its C-terminal isoform, Cx43-20k (Smyth and Shaw, 2013). Both Cx43-FL and Cx43-
359 20k are significantly decreased in Drp1 cKO astrocytes compared to cWT (Fig. 7J-K). These
360 findings indicate that loss of Drp1 dysregulates Cx43 protein, but not mRNA, expression in
361 astrocytes *in vivo*. Taken together, these data suggest that Drp1-induced mitochondrial fission is
362 required for proper Cx43 protein expression and the establishment of astrocyte organization in the
363 cortex.

DISCUSSION

Astrocytes require a highly complex morphology to perform essential roles in brain development. They ramify into hundreds of thousands of fine processes enabling their functional interaction with neurons, synapses, neighboring astrocytes, and other brain cells. Distal mitochondria locally interact with the cytoskeleton to regulate branch morphology in compartmentalized cells such as neurons (Courchet et al., 2013; Smith and Gallo, 2018), but the roles of mitochondria in fine astrocyte processes are largely unknown. Mature astrocytes were historically believed to be predominantly glycolytic (Pellerin and Magistretti, 1994), not depending on mitochondrial respiration for their own survival (Supplie et al., 2017), and instead using their mitochondria to provide metabolic support for neurons (Pellerin et al., 1998). Indeed, astrocyte mitochondria have recently emerged as gatekeepers of several biological processes that maintain brain homeostasis including regulation of blood-brain barrier remodeling, neuroinflammation, and neurodegeneration (Göbel et al., 2019; Ignatenko et al., 2018; Motori et al., 2013; Popov et al., 2023). While these studies introduce astrocytic mitochondria as key regulators of brain function, the cell-intrinsic roles of mitochondria in astrocyte and brain development are not well understood.

Our findings elucidate a previously unknown role for mitochondrial fission in regulating distal astrocyte process morphogenesis and astrocyte organization in the developing mouse cortex. We show that astrocytes undergo robust mitochondrial division to predominantly occupy distal astrocyte processes during postnatal cortical development. Inhibiting mitochondrial fission by silencing Drp1, reduces mitochondrial occupancy of distal astrocyte processes and diminishes peripheral astrocyte branch formation specifically, without affecting overall astrocyte territory size or growth. Functionally, Drp1-induced mitochondrial fission and occupancy of distal astrocyte processes are essential for the establishment of an organized astrocyte network and proper expression of gap junction protein, Cx43. Finally, mitochondrial fission is critical for astrocyte homeostasis, as global Drp1 loss in developing astrocytes induces cortical astrocyte reactivity, indicating that mitochondrial fission, distal mitochondrial localization, and astrocyte fine process formation are required for proper astrocyte development.

Several recent studies have elucidated astrocyte-neuron and astrocyte-astrocyte cell adhesion-based mechanisms that instruct astrocyte morphogenesis (Baldwin et al., 2021; Stogsdill et al., 2017; Takano et al., 2020; Tan et al., 2023; Zipursky et al., 2024). Curiously, loss of these cell-

394 adhesions often concurrently disrupts both astrocyte territory formation and complexity of distal
395 astrocyte processes. Here we identify an organelle-driven mechanism that regulates peripheral
396 astrocyte process morphogenesis independently from the development of higher order astrocyte
397 processes and overall astrocyte size. The specificity of mitochondrial fission in regulating distal
398 astrocyte process development could be attributed to their actin-rich cytoskeletal make-up which
399 is distinct from larger processes. Primary astrocyte processes, which determine territory size,
400 contain mainly intermediate filaments and microtubules (Haseleu et al., 2013). In other cell types,
401 local mitochondrial ATP has been shown to fuel actin polymerization (Cunniff et al., 2016). Thus,
402 it is possible that mitochondrial fission facilitates the recruitment of mitochondria into actin-rich
403 distal astrocyte processes to supply local ATP required for actin polymerization during
404 morphogenesis. In the absence of mitochondrial fission, the mislocalization of mitochondria away
405 from peripheral, fine astrocyte branchlets could impair actin-cytoskeleton dynamics during
406 morphogenesis. Because these peripheral astrocyte processes are critical components of the
407 tripartite synapse, future work is needed to elucidate the role of astrocyte mitochondrial fission in
408 proper synapse formation and function.

409 Our study establishes the role of Drp1 and mitochondrial fission in astrocyte organization in the
410 cortex as measured by the distances between astrocytic neighbors, and this disruption is likely
411 accompanied by tiling defects. While the molecular mechanisms that drive astrocyte domain
412 formation and tiling remain largely unknown, we know that proper organization of astrocyte
413 networks is functionally necessary for brain development and health. A recent study identified an
414 astrocyte-astrocyte cell-adhesion molecule, HepaCAM, that controls the establishment of non-
415 overlapping astrocyte domains through cis interactions with neighboring astrocytes and regulation
416 of Cx43 localization (Baldwin et al., 2021). In our study, both sparse knockdown and conditional
417 deletion of Drp1 in astrocytes led to dysregulation of Cx43 protein expression and caused disrupted
418 astrocyte organization in the cortex. These results support previous findings that both Cx43
419 abundance and stability are critical for the proper migration of astrocytes and even dispersion of
420 the astrocyte network (Lagos-Cabré et al., 2019; Wiencken-Barger et al., 2007), and reveal this
421 process is regulated at least in part by astrocyte mitochondrial fission during cortical development.
422 Future work is needed to investigate whether cortical astrocyte disorganization in response to Drp1
423 loss is also accompanied by disrupted astrocyte territory overlap and gap junction coupling.

How could Drp1-induced mitochondrial fission regulate Cx43 protein levels in astrocytes? Previous studies in cardiac cells found that the C-terminus of Connexin 43 is internally translated to generate a small 20kDa Cx43 isoform (Cx43-20kDa), which is required for the trafficking of full-length Cx43 (Cx43-FL) to the cell membrane (Smyth and Shaw, 2013). Loss of Cx43-20kDa leads to degradation of mistrafficked Cx-43-FL (Xiao et al., 2020). Importantly, Cx43-20kDa can localize to the outer mitochondrial membrane and in conditions of mitochondrial stress, which cause mitochondrial elongation, Cx43-20kDa can abandon its canonical Cx43-FL trafficking roles and instead employ a Drp1-independent, actin-based mechanism to induce mitochondrial fission (Shimura et al., 2021). Our findings show that conditional deletion of Drp1 in isolated astrocytes diminished both FL and the 20kDa isoforms of Cx43 protein. Importantly, Cx43 mRNA is unaffected by Drp1 loss, indicating Drp1 regulation of Cx43 occurs independently of transcription. Therefore, it is possible Drp1 loss in astrocytes causes a similar redirection of Cx43-20kDa away from its Cx43-FL trafficking role in an attempt to aid mitochondrial fission, resulting in the degradation of mistrafficked Cx43-FL and astrocyte disorganization. Furthermore, Cx43-20kDa has been previously detected in astrocytes and overexpression of astrocytic Cx43-20kDa promotes neuronal survival and recovery in a rat model of traumatic brain injury (TBI) through unknown mechanisms (Ren et al., 2020). These recent studies coupled with our findings suggest the Cx43-20kDa/Drp1 axis may be critical not only in brain development, but also in brain disease and therapeutics.

Finally, this study has important implications for understanding the pathology of neurological diseases, particularly neurodevelopmental diseases with Drp1 dysfunction. For example, point mutations in human Drp1 cause encephalopathy due to defective mitochondrial and peroxisomal fission-1 (EMPF1), a devastating disorder that presents in a spectrum of varying severity including microcephaly, developmental delay, refractory epilepsy, and lethal infantile encephalopathy (Fahrner et al., 2016; Lhuissier et al., 2022; Liu et al., 2021; Vanstone et al., 2016). While much research has focused on the disruption of excitation/inhibition (E/I) balance and neuronal pathogenesis of EMPF1 (Casillas-Espinosa et al., 2012; Ke et al., 2023), our results reveal how Drp1 dysfunction in astrocytes alone can fundamentally disrupt cortical development through astrocyte morphogenesis and organization deficits. Decreased distal astrocyte process development could contribute to diminished tripartite synapse formation (Stogsdill et al., 2017), subsequently disrupting the E/I balance. Furthermore, while loss of astrocyte tiling has been

455 reported in models of epilepsy (Oberheim et al., 2008), it has been unclear whether the phenotype
456 is causative or a consequence of disease. Our findings suggest endogenous loss of astrocytic Drp1
457 is sufficient to cause astrocyte reactivity which is a hallmark of many neurological disorders,
458 underscoring the translational importance of astrocyte mitochondrial fission in neuropathology. In
459 future studies, it will be interesting to investigate whether astrocyte-specific Drp1 loss causes the
460 synaptic E/I imbalance deficits associated with human *DNM1L* mutations. In conclusion, we show
461 a novel role for Drp1-induced mitochondrial fission in astrocyte peripheral process morphogenesis
462 and in regulating the establishment of an organized astrocyte network, demonstrating astrocyte
463 mitochondria are essential instructors of proper brain development.

464

465

466 **FIGURE LEGENDS**

467 **Fig.1: Mitochondria increase in number and decrease in size during cortical astrocyte**
468 **morphogenesis *in vivo*.** (A) Schematic of Postnatal Astrocyte Labeling by Electroporation
469 (PALE). (B) Representative images of V1 astrocytes expressing mCherry-CAAX (magenta, top
470 panels) and their EGFP mitochondria (green, bottom panels) at P4, P7, P14, and P21. Scale bar:
471 10 µm. Super-plots for the quantification of (C) astrocyte cell volume, (D) total mitochondrial
472 volume per cell, (E) mitochondrial volume normalized to cell volume, (F) average mitochondrial
473 number per cell, and (G) average mitochondrial size per cell from P4-P21. N=3-4 male and female
474 mice/timepoint (large circled data points), n= 2-6 cells/mouse, 10-13 cells total/timepoint (small
475 gray data points). Data are presented as mean ± SEM. Nested one-way ANOVA with Tukey post-
476 hoc test.

477 **Fig. 2: Mitochondria occupy fine astrocyte processes concurrently with astrocyte**
478 **morphological arborization *in vitro*.** (A) Schematic of astrocyte-neuron co-culture assay. (B)
479 Representative images of rat astrocytes transfected with EGFP (green, top panels) and MitoDsRed
480 (magenta, middle panels) from 4 to 48 hours in co-culture with cortical neurons. Inset (bottom
481 panels) of distal astrocyte processes (green) housing mitochondria (magenta) at the leading edge
482 of growing processes from 4 to 48 hours in culture. Scale bars: 20 µm. (C) Overview of Seg_Astro
483 image analysis pipeline. (D) Astrocyte secondary, fine/distal, and terminal branch number at 4 vs.
484 48 hours in culture. n = 10-12 cells per timepoint from one experiment. Unpaired two-tailed t-test.
485 (E) Total astrocyte mitochondria number, and (F) average mitochondrial size in secondary,
486 fine/distal, and terminal astrocyte branches from 4 to 48 hours in culture. n = 10-12 cells per
487 timepoint from one experiment. Data are presented as mean ± SEM. One-way ANOVA with Tukey
488 post-hoc test.

489 **Fig 3: Drp1-induced mitochondrial fission is required for fine astrocyte process formation**
490 **and mitochondrial localization *in vitro*.** (A) Schematic of Drp1 in mitochondrial fission. (B)
491 Drp1 domain structure noting K38E mutation in the GTPase domain. (C) Representative images
492 of rat astrocytes transfected with shRNA targeting Drp1 (shDrp1) or a scrambled control
493 (shControl) (first column) co-cultured on neurons (unlabeled), and their mitochondria (second
494 column) across primary, secondary, fine, and terminal astrocyte process types. Scale bar: 20µm.
495 (D) Super-plotted quantification of average mitochondrial number in secondary, fine, and terminal

496 branches from shControl vs. shDrp1 astrocytes. (E) Quantification of primary, secondary, fine, and
497 terminal branch numbers from shControl and shDrp1 astrocytes. Data are mean ± S.E.M. n = 4
498 independent experiments (large circles), 10 cells/condition/experiment (small gray dots). Nested
499 t-test. (F) Representative images of rat astrocytes transfected with shControl (green), shDrp1
500 (green), shDrp1 (green)+ hDrp1-YFP (magenta), or shDrp1 (green)+ hDrp1-K38E-CFP (magenta.
501 Scale bar: 40µm. (G) Quantification of total primary, (H) secondary, (I) fine, and (J) terminal
502 branch number in astrocytes across the 4 conditions from (F). Data are mean ± S.E.M. n = 3
503 independent experiments (large circles), 10 cells/condition/experiment (small gray dots). Nested
504 One-way ANOVA with Tukey post-hoc test.

505 **Fig 4: Mitochondrial fission, not fusion nor transport, is required for distal astrocyte process**
506 **morphogenesis *in vivo*.** (A, E, I) Schematic of mitochondrial fission, fusion, and transport
507 mediated by Drp1, Mfn1, and Miro1, respectively. (B-D, F-H, J-L) Representative images of V1
508 P21 astrocytes expressing mCherry-CAAX-tagged shRNA (magenta) against Drp1 (shDrp1),
509 Mfn1 (shMfn1), Miro1, (shMiro1) or scrambled control (shControl) and their EGFP mitochondria
510 (green). Scale bar, 10µm. (B, F, J) Astrocyte territory (cyan) and quantification, (D, G, K) NIV
511 reconstructions (cyan) and quantification, and (D, H, L) distal mitochondrial volume (green within
512 cyan ROI) and quantification in shControl, shDrp1, shMfn1, and shMiro1 conditions, respectively.
513 N= 4-5 male and female mice/condition (large circles), n=2-4 cells/mouse, 10-15 cells
514 total/condition (small gray dots). Data are mean ± S.E.M. Nested t-test.

515 **Fig 5: Drp1 controls cortical astrocyte organization during postnatal development.** (A)
516 Representative images of V1 mouse cortices with astrocytes expressing mCherry-CAAX-tagged
517 shRNA (magenta) against Drp1 (shDrp1) or scrambled control (shControl) and their EGFP
518 mitochondria (green) at P7, P14, and P21. Scale bar, 200µm. (B) Quantification of astrocyte
519 individual or cluster area per field of view at P7, P14, P21. N=3-4 male and female mice/condition
520 (big circles), 3 cortical sections/mouse (small gray dots). Data points are mean ± S.E.M. Nested t-
521 test. (C) Representative images of shControl (top) and shDrp1 (bottom) P21 astrocytes expressing
522 mCherry-CAAX shRNAs (magenta) and stained with Sox9 (green). Yellow arrows note Sox9+
523 astrocytic nuclei within mCherry+ astrocytes. Scale bar, 40µm. (D) Quantification of number of
524 Sox9+ astrocyte nuclei and (E) nearest neighbor distance between astrocytes per astrocyte cluster
525 in P21 shControl and shDrp1 astrocytes. N=4-5 male and female mice/condition (large circles),
526 n=2-6 cells or clusters/condition, 20 cells or clusters total/condition (small gray dots). Data are

527 mean ± S.E.M. Nested t-test. (F) Representative images of V1 astrocytes expressing mCherry-
528 CAAX and shControl (top) and shDrp1 (bottom) stained with Cx43 (cyan) at P21. Scale bars,
529 20µm. (G) Quantification of Connexin43 expression within mCherry-CAAX astrocytes. N=6 male
530 and female animals/condition (large circles), n=2-6 cells or clusters/animal, 20-25 cells
531 total/condition (small gray dots). Data are mean ± S.E.M. Nested t-test.

532 **Fig 6: Astrocyte-specific Drp1 cKO induces cortical astrocyte reactivity.**

533 (A) Overview of astrocyte-specific conditional Drp1 knockout mouse breeding strategy and
534 timeline of tamoxifen administration. (B) Representative immunoblot for Drp1 from immuno-
535 purified astrocytes. COX4, a mitochondrial protein, serves as a loading control. (C) Quantification
536 of Drp1 protein in isolated cKO and cWT astrocytes. N=3 mice/condition. Data are mean ± S.E.M.
537 Unpaired, two-tailed t-test. (D) Representative images of Drp1 cWT and cKO V1 cortices at P21
538 with tdTomato$^+$ astrocytes (magenta, first column), stained for GFAP (green, second column), and
539 merge (third column). Scale bar, 100µm. Zoom merge (last column). Scale bar, 20µm. (E)
540 Quantification of cortical tdTomato$^+$ soma count of astrocyte density, (F) tdTomato$^+$ astrocyte
541 coverage normalized to astrocyte density, (G) GFAP soma count, and (H) GFAP coverage
542 normalized to astrocyte density per layer in Drp1 cKO compared to cWT. N=4 male and female
543 mice/condition, 2-3 cortical images/mouse. Data are mean ± S.E.M. Two-way ANOVA with
544 Sidak's multiple comparisons test.

545 **Fig 7: Astrocytic Drp1 loss dysregulates astrocyte organization and Connexin 43 expression**
546 **in the mouse cortex.** (A) Diagram of astrocyte organization analysis by nearest and multiple
547 neighbor distance quantification. (B) Violin plot of nearest neighbor average distance between
548 tdTomato$^+$ somas across V1 cortex of Drp1 cWT and cKO mice. N=4 male and female
549 mice/condition (large circles), ~200 distances per image, 2-3 cortical images/mouse. Data are
550 mean ± S.E.M. Nested t-test. (C) Distribution of average distances to multiple (9) neighbors. N=4
551 male and female mice/condition, ~200 distances per image, 2-3 images/mouse. Kolmogorov-
552 Smirnov test. (D) Representative images of Drp1 cWT and cKO V1 cortices with tdTomato$^+$
553 astrocytes (magenta) stained with Cx43 (cyan) at P21. Scale bar, 100µm. Quantification of (E)
554 individual (F) variance, and (G) distribution of Cx43 mean gray value per astrocyte in Drp1 cKO
555 and cWT mice. N=4 male and female mice/condition, n= 15-30 mid-layer astrocytes (L2/3, L4,
556 L5) per animal from 2-3 section images/animal. Nested t-test for (E), Unpaired, two-tailed t-test

557 for (F), and Kolmogorov-Smirnov test for (G). (H) Quantification of Cx43 mRNA from isolated
558 cKO and cWT astrocytes. N=4-6 mice/condition. Data are mean ± S.E.M. Unpaired two-tailed t-
559 test. (I) Representative immunoblot of isolated astrocytes for Cx43 showing its full-length form at
560 40kDa and its 20kDa isoform using COX4 as loading control. (J) Quantification of full-length
561 Cx43 protein, (K) Cx43-20kDa isoform protein in isolated cKO and cWT astrocytes. N=3
562 mice/condition. Data are mean ± S.E.M. Unpaired, two-tailed t-test.

563 **Supplemental Figure 1: Validation of shRNA tools**

564 **(A)** Schematic of shDrp1 sequence aligned to the mouse, rat, and human genome. **(B)** Drp1 relative
565 mRNA expression in control and shDrp1 transfected mouse 3T3 cells. **(C)** Schematic of shMiro1
566 and shMfn1 sequences aligned to the mouse genome. **(B)** Miro1 and Mfn1 relative mRNA
567 expression in control and shDrp1 transfected mouse 3T3 cells. Data are mean ±S.E.M. n = 3
568 independent experiments. Unpaired two-tailed t-test.

569 **Supplemental Figure 2: Mitochondrial dynamics do not affect astrocyte total mitochondrial**
570 **content**

571 (A) Representative images of Imaris reconstructed V1 P21 astrocytes expressing mCherry-CAAX-
572 tagged shRNA (magenta) against Drp1 (shDrp1), Mfn1 (shMfn1), Miro1, (shMiro1) or scrambled
573 control (shControl) and their EGFP mitochondria (green). Scale bar, 10µm. **(B-D)** Quantification
574 of total mitochondrial volume normalized to cell volume in shDrp1, shMfn1, and shMiro1
575 conditions, respectively. N=4-5 male and female mice/condition (large circles), n=2-4 cells/mouse,
576 10-15 cells total/condition (small gray dots). Data are mean ± S.E.M. Nested t-test.

577 **Supplemental Figure 3: shDrp1-induced astrocyte clustering is not a result of increased**
578 **astrocyte proliferation and is maintained through adulthood**

579 **(A)** Overview of PALE combined with EdU labeling. **(B)** Representative images of V1 cortices
580 with astrocytes expressing mCherry-CAAX shRNA (red) against Drp1 (shDrp1) or scrambled
581 control (shControl) and EdU labeling (magenta) at P4 and P14. Scale bar, 200µm. **(C)**
582 Quantification of Edu+ cells in shControl or shDrp1 cortices at P4, P8, P10, P12, and P14. N=3-4
583 male and female mice/condition, 3 cortical section images/mouse. Data points are timepoint
584 averages ± S.E.M. Two-way ANOVA with Sidak's multiple comparisons test. **(D)** Representative
585 images of V1 cortices with astrocytes expressing mCherry-CAAX shRNA (magenta) against Drp1

586 (shDrp1) or scrambled control (shControl) at 2 months and 6 months. Scale bar, 200µm. **(E)**
587 Quantification of astrocyte cell or cluster area per field of view at 2 and 6 months. N=3 male and
588 female mice/condition (large circles), 3 cortical section images/mouse (small gray dots). Data
589 points are mean ± S.E.M. Nested t-test. **(F)** Representative images of V1 astrocytes from 3 mice
590 per condition expressing mCherry-CAAX and shControl (top two rows) and shDrp1 (bottom two
591 rows) stained with an antibody against Cx30 (cyan) at P21. Scale bars, 20µm.

592 **Supplemental Figure 4: Astrocyte-specific Drp1 cKO mouse characterization**

593 (A) Representative images of Drp1 cWT and cKO V1 cortices with tdTomato^{+} astrocytes
594 (magenta) stained with Drp1 (yellow) and showing Drp1 masked by tdTomato (last column) at
595 P21. Scale Bar, 40µm. (B-C) Quantification of Drp1 mean gray value within tdTomato area
596 normalized to astrocyte density per cortical layer (B) and across the whole cortex (C). N=3-4 male
597 and female mice/condition, 2-3 cortical images/mouse. Data points are mean ± S.E.M. Two-way
598 ANOVA with Sidak's multiple comparisons test for B, and Unpaired, two-tailed t-test for C. (D)
599 Quantification of cortical thickness in Drp1 cKO compared to cWT mice. N=4 male and female
600 mice/condition (large circles), n=2-3 cortical images/mouse (small gray dots). Data are mean ±
601 S.E.M. Unpaired, two-tailed t-test. Quantification of (E) GFAP and (F) Vimentin mRNA from
602 isolated cKO and cWT astrocytes. N=2-6 male and female mice/condition. Data are mean ± S.E.M.
603 Unpaired two-tailed t-test.

604 **MATERIALS AND METHODS**

605 **Resource availability**

606 Further information and requests for resources and reagents should be directed to and will be
607 fulfilled by Cagla Eroglu (cagla.eroglu@duke.edu).

608 **Materials availability**

609 The reagents generated in this study are available without restriction.

610 **Data and code availability**

611 The raw data and analyses generated during this study can be accessed on Zenodo at the following
612 DOI: 10.5281/zenodo.13961281. The Seg_Astro code can be found at (https://github.com/Eroglu-
613 Lab/seg_cul_astro_app/tree/main). Any additional information can be requested from the lead
614 contact.

615 **Animal studies**

616 All mice and rats were used in accordance with the Institutional Animal Care and Use Committee
617 (IACUC) and with oversight by the Duke Division of Laboratory Animal Resources (IACUC
618 Protocol Numbers A117-20-05 and A103-23-04). All animals were housed under typical 12-hour
619 light/dark cycles. Aldh1l1-Cre/ERT2 BAC transgenic (RRID:IMSR_JAX:029655) and ROSA-td-
620 Tomato Ai14 (RTM) (RRID:IMSR_JAX:007914) lines were obtained through Jackson
621 Laboratory. Wild-type CD1 mice (RRID: IMSR_CRL:022) used for PALE and CD1 (Sprague-
622 Dawley) IGS rats (SD-001) used for primary culture preps were purchased from Charles River
623 Laboratories. Rosa26-lsl-mito-EGFP (RRID:IMSR_JAX:021429) were previously described
624 (Agarwal et al., 2017). Drp1 conditional knockout mice were previously described and were a gift
625 from the Sesaki Laboratory (Wakabayashi et al., 2009a). Mice and rats of both sexes were included
626 in all experiments. Sex was not an influence on any of the experimental outcomes.

627 **Primary Cultures**

628 *Cortical Neuron Isolation and Culture* Purified (glia-free) rat cortical neurons were prepared as
629 described previously (Stogsdill et al., 2017). In brief, cortices from P1 rat pups of both sexes

630 (Sprague Dawley, Charles River Laboratories, SD-001) were micro-dissected, digested in papain
631 (~7.5 units/mL) at 33°C for 45 minutes, triturated in low and high ovomucoid solutions,
632 resuspended in panning buffer (DPBS (Gibco 14287) supplemented with BSA and insulin) and
633 passed through a 20 µm mesh filter (Elko Filtering 03-20/14). Filtered cells were incubated on
634 negative panning dishes coated with Bandeiraea Simplicifolia Lectin 1 (x2), followed by goat anti-
635 mouse IgG+IgM (H+L) (RRID: AB_2338451), and goat anti-rat IgG+IgM (H+L)
636 (RRID:AB_2338094) antibodies, then incubated on positive panning dishes coated with mouse
637 anti-L1 (RRID:AB_528349) to bind cortical neurons. Adherent cells were collected by forceful
638 pipetting with a P1000 pipette. Isolated neurons were pelleted (11 min at 200 g) and resuspended
639 in serum-free neuron growth media (NGM; Neurobasal, B27 supplement, 2 mM L-Glutamine, 100
640 U/mL Pen/Strep, 1 mM sodium pyruvate, 4.2 µg/mL Forskolin, 50 ng/mL BDNF, and 10 ng/mL
641 CNTF). 100,000 neurons were plated onto 12 mm glass coverslips coated with 10 µg/mL poly-D-
642 lysine (PDL, Sigma P6407) and 2 µg/mL laminin and incubated at 37°C in 10% CO2. On day in-
643 vitro (DIV) 2, half of the media was replaced with NGM Plus (Neurobasal Plus, B27 Plus, 100
644 U/mL Pen/Strep, 1 mM sodium pyruvate, 4.2 µg/mL Forskolin, 50 ng/mL, BDNF, and 10 ng/mL
645 CNTF) and AraC (10 µM, Sigma, C1768) was added to stop the growth of proliferating
646 contaminating cells. On DIV 3, all of the media was replaced with NGM Plus. Neurons were fed
647 on DIV 6 and DIV 9 by replacing half of the media with NGM Plus. Detailed protocol can be
648 found at (https://www.protocols.io/view/glia-free-cortical-neuron-culture-36wgq3r35lk5/v1)

649 *Cortical Astrocyte Isolation and Culture* Rat cortical astrocytes were prepared as described
650 previously (Stogsdill et al., 2017). Briefly, P1 rat cortices from both sexes were micro-dissected,
651 papain digested, triturated in low and high ovomucoid solutions, and resuspended in astrocyte
652 growth media (AGM: DMEM (Gibco 11960), 10% FBS, 10 µM, hydrocortisone, 100 U/mL
653 Pen/Strep, 2 mM L-Glutamine, 5 µg/mL Insulin, 1 mM Na Pyruvate, 5 µg/mL N-Acetyl-L-
654 cysteine). Between 15-20 million cells were plated on 75 mm2 flasks (non-ventilated cap) coated
655 with poly-D-lysine and incubated at 37°C in 10% CO2. On DIV 3, removal of non-astrocyte cells
656 was performed by forcefully shaking closed flasks by hand for 10-15 seconds until only an
657 adherent monolayer of astrocytes remained. AraC was added to the media from DIV 5 to DIV 7 to
658 eliminate contaminating fibroblasts. On DIV 7, astrocytes were trypsinized (0.05% Trypsin-
659 EDTA) and plated into 12-well or 6-well dishes. On DIV 8, cultured rat astrocytes were transfected

660 with shRNA and/or expression plasmids using Lipofectamine LTX with Plus Reagent (Thermo
661 Scientific, 15338100) per the manufacturer's protocol. Briefly, 1 µg (12-well) or 2 µg (6-well) total
662 DNA was diluted in Opti-MEM containing Plus Reagent, mixed with Opti-MEM containing LTX
663 (1:2 DNA to LTX) and incubated for 30 minutes. The transfection solution was added to astrocyte
664 cultures and incubated at 37°C for 3 hours. On DIV 10, astrocytes were trypsinized, resuspended
665 in NGM plus, plated (20,000 cells per well) onto DIV 10 neurons, and co-cultured for 48 hours.
666 Detailed protocol can be found at (https://www.protocols.io/view/astrocyte-isolation-and-acm-
667 production-261gedp57v47/v1).

668 **Cell Lines**

669 *3T3* 3T3 cells (RRID:CVCL_0594) used for shRNA validation experiments were cultured in
670 DMEM supplemented with 10% fetal bovine serum, 100 U/mL Pen/Strep, 2 mM L-Glutamine,
671 and 1 mM sodium pyruvate. Cells were incubated at 37°C in 5% CO2 and passaged every 2-3
672 days.

673 **Plasmids**

674 *shRNA plasmids* pLKO.1 puro plasmids containing shRNA against mouse/rat *Drp1*
675 (TRCN0000321170; CTATAATGCATGCACTATTTA) was generated in this study. shRNA
676 sequence was obtained from RNAi Consortium (TRC) via Dharmacon. A scrambled shRNA
677 sequence was generated (GTTCTAAGTTCCGTGTTCAGG) and cloned into the pLKO.1 TRC
678 cloning vector (Moffat et al., 2006) according to Addgene protocols
679 (https://www.addgene.org/protocols/plko/). To generate pLKO.1 shRNA plasmids that express
680 EGFP, CAG-EGFP was removed from pLenLox-shNL1-CAG-EGFP (Chih et al., 2006) and
681 inserted between Kpn1 and Spel sites in pLKO.1 Puro, replacing the puromycin resistance gene in
682 pLKO.1. Final constructs generated were pLKO.1-scrambled-GFP (RRID: Addgene_228736) and
683 pLKO.1-shDrp1-GFP (RRID: Addgene_228737).

684 *PiggyBac plasmids* pGLAST-PBase was a gift from Dr. Joseph Loturco (Chen and LoTurco, 2012).
685 shRNA sequences against mouse/rat *Miro1* (TRCN0000330651;
686 TGGACTGTGCTTCGACGATTT), *Mfn1* (TRCN0000081400;
687 GCAAGATTACAGGAGTTTCAA), and *Drp1* (see above *shRNA plasmids*) were obtained from

688 RNAi Consortium (TRC) via Dharmacon. A scrambled shRNA sequence was generated (see above
689 *shRNA plasmids*). To insert the hU6 promoter and shRNA in pPBCAG-mCherry-CAAX a DNA
690 fragment containing hU6 and shRNA was amplified from pLKO.1-shRNA using Phusion High-
691 Fidelity DNA Polymerase (NEB) with primers that introduced SpeI restriction sites (Forward
692 Primer: GGACTAGTCAGGCCCGAAGGAATAGAAG; Reverse Primer:
693 GGACTAGTGCCAAAGTGGATCTCTGCTG). PCR products were purified, digested with SpeI,
694 and ligated into pPBCAG-mCherry-CAAX at the SpeI restriction site. An analytical digest with
695 EcoRI followed by sequencing was used to confirm the orientation of the inserted DNA fragment.
696 Final plasmids generated were pPB-scrambled-mCherry-CAAX (RRID: Addgene_228738), pPB-
697 sDrp1-mCherry-CAAX (RRID: Addgene_228739), pPB-shMiro1-mCherry-CAAX (RRID:
698 Addgene_228741), and pPB-shMfn1-mCherry-CAAX (RRID: Addgene_228740).

699 *Other plasmids* hDrp1-YFP and hDrp1-K38E-CFP were gifts from Heidi McBride (König et al.,
700 2021) . Mito-DsRed was acquired from Addgene (RRID: Addgene_55838).

701 **Biochemical assays**

702 *mRNA extraction and cDNA preparation* Cells stored in TRIzol (#15596026; Invitrogen) were
703 brought to room temperature and resuspended in a final volume of 1 ml of TRIzol. 200 µl of
704 chloroform was added to each sample and mixed thoroughly. Samples were centrifuged at 12,000
705 g for 15 min at 4°C for phase separation and the clear aqueous phase was collected. 2 µl of
706 GlycoBlue Coprecipitant (15 mg/ml, #AM9515; Invitrogen) and 500 µl of isopropanol were added
707 to each sample, centrifuged at 12,000 g for 10 min at 4°C, precipitating RNA as a blue pellet. The
708 RNA pellet was rinsed in 75% ethanol, air-dried, and resuspended in 20 µl of nuclease-free water.
709 mRNA concentration in each sample was quantified via Qubit RNA HS Assay Kit (#Q32852;
710 Invitrogen). RNA samples were then diluted with nuclease-free water to match concentrations
711 across all samples. cDNA libraries were then generated by incubating the samples with qScript
712 cDNA SuperMix (#101414-102; VWR) and nuclease-free water for 5 min at 25°C, 30 min at 42°C,
713 and 5 min at 85°C. The resulting cDNA was then diluted appropriately with nuclease-free water
714 and stored at −80°C.

715 *Real-time qPCR* cDNA samples were plated in duplicate on a 96-well qPCR plate and incubated
716 with Fast SYBR Green Master Mix (#4385616; Applied Biosystems), nuclease-free water, and
717 the forward and reverse primers of interest at a ratio of 5 µl SYBR: 3 µl water: 0.5 µl forward
718 primer: 0.5 µl reverse primer: 1 µl sample. Each sample was plated twice to ensure technical
719 replicates. A no-cDNA sample (water with primers and Master Mix) served as a negative control.
720 Cycle threshold values were collected for each well and normalized to PPIA as a housekeeping
721 gene. The sequences of forward (F) and reverse (R) primers used (5′→ 3′) are:
722 Drp1: (F) TTACGGTTCCCTAAACTTCACG and (R) GTCACGGGCAACCTTTTACGA
723 Miro1: (F) TGGGCAGCACTGATAGAATAGA and (R) GCAAAGACCGTAGCACCAAAG
724 Mfn1: (F) CCTACTGCTCCTTCTAACCCA and (R) AGGGACGCCAATCCTGTGA
725 Cx43: (F) ACAGCGGTTGAGTCAGCTTG and (R) GAGAGATGGGGAAGGACTTGT
726 GFAP: (F) GGGGCAAAAGCACCAAAGAAG and (R) GGGACAACTTGTATTGTGAGCC
727 Vimentin: (F) CGTCCACACGCACCTACAG and (R) GGGGGATGAGGAATAGAGGCT
728 PPIA: (F) GAGCTGTTTGCAGACAAAGTTC and (R) CCCTGGCACATGAATCCTGG

729 *Protein extraction and western blotting* Protein was extracted from cultured cells using RIPA lysis
730 buffer (ThermoFisher, 89900). Cells were washed twice with ice-cold DPBS and incubated on ice
731 in RIPA buffer for 5 minutes with occasional agitation. Cell lysates were collected, vortexed
732 briefly, and centrifuged at 4°C at high speed for 10 minutes to pellet non-solubilized material. The
733 supernatant was collected and stored at −80°C. To collect protein from astrocytes from Drp1 *cWT*
734 and *cKO* mice at P21, astrocytes were isolated following a modified version of the Magnetic
735 Activated Cell Sorting (MACS) protocol previously described (Holt et al., 2019). In brief, mice
736 were anesthetized with 200 mg/kg tribromoethanol (avertin) and perfused with TBS/Heparin,
737 cortices rapidly dissected, digested in papain (~7.5 units/mL) at 33°C for 45 minutes with pipette
738 trituration every 15 minutes. Then homogenates were resuspended in Magnetic Activated Cell
739 Sorting (MACS) buffer (0.002M EDTA, 0.2% milk peptone, 0.01M HEPES pH 7, 0.5% Glucose,
740 1X HBSS), and passed through a CellTrics 30 µm filter (Sysmex, 04-004-2326). Cortical cells
741 were then cleared from microglia by incubating with anti-CD11b human/mouse magnetic
742 microbeads (Miltenyi Biotec, 130-093-634) for 10 minutes at 4°C with rotation and passed through
743 an LS separation column (Miltenyi Biotec, 130-042-401) inserted into a Quadro MACS Multi
744 Stand magnetic stand (Miltenyi Biotec) followed by 3 washes with MACS buffer. Flowthrough

745 was then spun down and resuspended in MACS buffer and incubated with blocking buffer and
746 anti-ACSA2 mouse magnetic microbeads (Miltenyi Biotec, 130-097-678) for 30 minutes at 4°C
747 with rotation to isolate astrocytes. Cell suspension was again passed through a separation column
748 inserted into a magnetic stand, rinsed 3 times with MACS buffer and column retentate (ACSA2+
749 population, astrocytes) was pelleted. Supernatant was discarded and astrocyte pellet was
750 resuspended in RIPA buffer containing protease inhibitors (Roche, 4693132001) and incubated
751 with rotation at 4°C for 20 minutes. Lysate was centrifuged at max speed at 4°C for 10 minutes,
752 supernatant collected and stored at −80°C.

753 Pierce Micro BCA Protein Assay Kit (Thermo Fisher, 23235) was used to determine protein
754 concentration, and lysates were subjected to western blot analysis and quantification using a
755 SimpleWestern Jess (ProteinSimple) automated immunoassay system with a 12-230kDa
756 Chemiluminescence Separation module (SM-W001) and associated manufacturer's protocol.
757 Primary antibodies used were: anti-Drp1 (Rabbit,1:10, RRID: AB_2895215), Connexin43 (Rabbit,
758 1:10, RRID:AB_2294590), COX4 (Rabbit, 1:10, RRID:AB_443304).

759 **Immunocytochemistry**

760 Astrocyte-neuron co-cultures on glass coverslips were fixed on DIV 12 with warm 4% PFA for 7
761 minutes, washed 3 times with PBS, blocked in a blocking buffer containing 50% normal goat
762 serum (NGS) and 0.4% Triton-X 100 for 30 minutes, and washed in PBS. Samples were then
763 incubated overnight at 4°C in primary antibodies diluted in blocking buffer containing 10% NGS.
764 Primary antibodies used were: anti-GFP (Chicken, 1:1000, RRID:AB_10000240) and anti-RFP
765 (Rabbit, 1:1000, RRID:AB_2209751). Cells were then washed with PBS, incubated in Alexa-
766 Fluor conjugated secondary antibodies (Life Technologies) for 2 hours at room temperature, and
767 washed again in PBS. Coverslips were mounted onto glass slides with Vectashield mounting media
768 containing DAPI (Vector Labs, H-1200-10), sealed with nail polish, and imaged on a BZ-X800
769 microscope (Keyence). Images of astrocytes were acquired at 40x magnification in red, green,
770 and/or DAPI channels using a CCD camera. Astrocytes that contained a single nucleus as revealed
771 by DAPI stain, strongly expressed fluorescent markers, and were not overlapping with other
772 labeled astrocytes, were selected for imaging.

773 Astrocyte branch number and mitochondrial localization were analyzed using Seg_Astro
774 MATLAB plugin. To quantify branch and mitochondrial number and size across the astrocyte
775 arbor, Seg_Astro (https://github.com/Eroglu-Lab/seg_cul_astro_app/tree/main) first detects the
776 astrocyte as well as the mitochondria by identifying locally significant regions based on order
777 statistics(Wang et al., 2020). Specifically, for the detection of the astrocyte, due to the nonuniform
778 intensity inside the cell, the initial detection contained many fragments. We further refined the
779 detection by searching for the globally optimal linkage, which is based on the graph design that
780 each node represents a fragment and the edge weight between nodes represents the mean intensity
781 of the brightest path between each pair of fragments. Then, the optimal linkage was obtained by
782 finding the min-spanning tree of the graph. Once the astrocyte is detected, Seg_Astro then uses
783 branch width and branchpoints to determine the astrocyte branch hierarchy and assign four types
784 of astrocyte branches per cell: 1) soma and primary processes, 2) secondary processes, 3) fine
785 processes, and 4) the terminal tips of processes (Fig. 2C). Seg_Astro then bins mitochondria into
786 these 4 branch types and outputs branch number, mitochondrial number, and mitochondrial size
787 per branch type. Importantly, we excluded mitochondrial measurements from the soma and
788 primary branches of astrocytes as mitochondria form a dense network in these compartments that
789 cannot be distinguished as discrete mitochondria for number and size quantification. Image
790 acquisition and analysis were performed blinded to experimental conditions. Each independent
791 experiment consisted of primary neurons and astrocytes isolated from a unique litter of wild-type
792 rats of mixed sexes. The exact number of independent experiments and the exact number of cells
793 analyzed are indicated in the figure legend for each experiment. Branch and mitochondrial number
794 per conditions were statistically analyzed using nested t-test or nested one-way ANOVA on
795 Graphpad Prism 9.

796 **Postnatal Astrocyte Labeling by Electroporation (PALE)**

797 Late P0/early P1 mice were sedated by hypothermia until anesthetized and 1 µL of plasmid DNA
798 mixed with Fast Green Dye was injected into the lateral ventricle of one hemisphere using a pulled
799 glass pipette. For mCherryCAAX labeling and shRNA knockdown experiments in pups from mito-
800 EGFP mice crossed with wild-type CD1 mice, the 1 µL of DNA contained 0.8 µg of pGLAST-
801 PBase, 0.7 µg of pPB-shRNA-mCherryCAAX, and 0.5 µg of pCAG-Cre (RRID:
802 Addgene_13775). Following DNA injection, electrodes were oriented with the positive terminal

803 above the visual cortex and the negative terminal below the chin, and 5 discrete 50 msec pulses of
804 100 V spaced 950 msec apart were applied. Pups were recovered on a heating pad, returned to their
805 home cage, and monitored until collection at P4, P7, P14, P21, P60, or P180. In the case of plasmid
806 expression in CD1 mice, assignment to experimental groups was randomly determined for each
807 litter. The number of replicates for each experiment is indicated in the figure legends. All animals
808 that appeared healthy at the time of collection were processed for data collection. All brain sections
809 were examined for the presence of electroporated cells before staining and downstream analyses.

810 **Tamoxifen administration**

811 Tamoxifen (Sigma, T5648) was dissolved in corn oil (Sigma, 8267) at a concentration of 10 mg/mL
812 and further diluted in corn oil to 1.25 mg/mL. 40 μL of the tamoxifen solution was injected into
813 the milk spot using an insulin syringe, for a dose of 0.05 mg at P1, P2, and P3. Two tamoxifen
814 injections (P1 and P2) were sufficient turn on tdTomato expression in all astrocytes, however a
815 third dose of tamoxifen (at P3) was needed for achieving a significant decrease of Drp1 levels in
816 astrocytes.

817 **EdU administration**

818 EdU stock solution from Click-iT EdU Imaging Kit (Thermofisher, C10640) was diluted in DPBS
819 to a concentration of 10μM (2.5μg of EdU/μl). At timepoints noted in Supplemental Figure 4, pups
820 were weighed and injected with 15μg of EdU per gram of animal weight (6μl of working 10μM
821 EdU stock solution per gram of animal weight). Animals were collected for staining 16 hours after
822 EdU injection and tissue sections were stained following the Click-iT EdU Imaging Kit
823 manufacturer protocol.

824 **Immunohistochemistry**

825 *Sample Preparation* Mice used for immunohistochemistry were anesthetized with 200 mg/kg
826 tribromoethanol (avertin) and perfused with TBS/Heparin and 4% PFA. Brains were collected and
827 post-fixed in 4% PFA overnight, cryoprotected in 30% sucrose, frozen in a solution containing 2
828 parts 30% sucrose and 1 part TissueTek O.C.T. (Sakura Finetek, cat#4583) and stored at −80°C.
829 Floating coronal tissue sections of 30, 40, 100 μm thickness were collected and stored in a 1:1

830 mixture of TBS/glycerol at −20°C. For immunostaining, sections were washed in 1x TBS
831 containing 0.2% Triton-X 100 (TBST), blocked in 10% NGS diluted in TBST, and incubated in
832 primary antibody for 2-3 nights at 4°C with shaking. Primary antibodies used were: anti-RFP
833 (Rabbit, 1:2000, RRID:AB_2209751), GFP (Chicken, 1:2000, RRID:AB_10000240), Sox9
834 (Rabbit, 1:2000, RRID:AB_2239761), Connexin43 (Rabbit, 1:100, RRID:AB_2294590), Drp1
835 (Mouse, 1:100, RRID:AB_398424), Connexin30 (Rabbit, 1:500, RRID:AB_2533979), and GFAP
836 (Rabbit, 1:1000, RID:AB_10013382). Following primary incubation, sections were washed in
837 TBST, incubated in Alexa-Fluor conjugated secondary antibodies diluted 1:200 (Life
838 Technologies) for 2-3 hours at room temperature, washed with TBST, and mounted onto glass
839 slides using a homemade mounting media (90% Glycerol, 20 mM Tris pH 8.0, 0.5% n-Propyl
840 gallate) and sealed with nail polish. For primary antibodies produced in mouse, isotype specific
841 secondary antibodies were always used (e.g. goat anti-mouse IgG1) to avoid excessive background
842 staining. For DAPI staining, DAPI (1:50,000) was added to the secondary antibody solution for
843 the final 10 minutes of incubation. Images were acquired on a Stellaris 8 Leica microscope.

844 *Astrocyte territory volume analysis* To assess the territory volume of individual astrocytes in the
845 developing mouse cortex, 100 µm-thick floating sections containing V1 astrocytes labeled sparsely
846 via PALE with mCherry-CAAX and mito-EGFP were collected. High magnification images
847 containing an entire astrocyte (50-60 µm Z-stack) were acquired on the Olympus FV 3000
848 microscope with the 60x objective. Criteria for data inclusion required that the entirety of the
849 astrocyte could be captured within a single brain section, and that the astrocyte was located in
850 layers 2/3, 4, or 5 of the visual cortex. Astrocytes in which the entire astrocyte could not be
851 captured within the section or were located in other layers or outside of the visual cortex were
852 excluded from the study and not imaged. Imaged astrocytes were analyzed using Imaris Bitplane
853 software as described previously (Stogsdill et al., 2017). Briefly, surface reconstructions were
854 generated and the Imaris Xtensions "Visualize Surface Spots" and "Convex Hull" were used to
855 create an additional surface render representing the territory of the astrocyte. The volume of each
856 territory was recorded, and astrocyte territory sizes from biological replicates were analyzed across
857 experimental conditions using a nested t-test. The number of mice and cells/mouse analyzed are
858 specified in the figure legend for each experiment.

859 *Neuropil infiltration volume analysis* To measure the extent of astrocyte infiltration into the
860 neuropil, 60x high magnification Z-stack images with 2x optical zoom were acquired from
861 mCherry-CAAX and mito-EGFP labeled astrocytes in 40 µm brain sections. Criteria for inclusion
862 required the astrocyte to be located within layer 2/3, 4, or 5 of the visual cortex, express the
863 fluorescent label, include their soma in the z-stack capture, and have at least 15µm in the z-
864 dimension contained within the section. Astrocytes that did not meet these criteria were excluded
865 from the study and not imaged. For each astrocyte, three ROIs (12.65 µm x 12.65 µm x 10 µm)
866 containing the neuropil, and devoid of cell soma, large branches, and end feet were chosen and
867 reconstructed using the surface tool in Imaris. The surface volume of each ROI was calculated and
868 the three data points from each astrocyte were averaged. Data from biological replicates were
869 analyzed using a nested t-test. The number of mice and cells/mouse analyzed are specified in the
870 figure legend for each experiment.

871 *Mitochondrial volume analysis* To measure mitochondrial volume within whole astrocytes or distal
872 astrocyte process, astrocyte images were captured as described above in *Astrocyte territory volume*
873 *analysis* (for whole astrocyte mitochondrial volume) or *Neuropil infiltration volume analysis* (for
874 distal NIV mitochondrial volume). In Imaris, the astrocyte volume rendered above was used to
875 mask the mitochondrial EGFP channel. Either whole or distal mitochondria were reconstructed
876 using the surface volume tool in Imaris. Data from biological replicates were analyzed using a
877 nested t-test. The number of mice and cells/mouse analyzed are specified in the figure legend for
878 each experiment.

879 *Quantification of astrocyte cell or cluster area* To analyze astrocyte cell or cluster area of sparse
880 Drp1 knockdown PALE experiments, three 40µm sections per animal were imaged in 10x on the
881 Olympus FV 3000 and loaded into ImageJ. The astrocyte mCherry channel, the RFP channel, was
882 selected. The image was then stacked into a max projection z-stack and a gaussian blur of sigma
883 radius 1.00 was applied. A threshold was then applied to the image to include signal from
884 astrocytes in the cortex above the subventricular zone. Then, using ImageJ analysis, the area of
885 each cluster above 500 pixels per image was recorded. The average cluster area per image was
886 calculated and 3 technical replicates per animal were averaged for analysis. Data from biological
887 replicates were analyzed using a nested t-test. The number of mice and cells/mouse analyzed are
888 specified in the figure legend for each experiment.

889 *Nearest and multiple neighbor analysis* To measure the distance between astrocyte neighbors in
890 sparse Drp1 knockdown PALE experiments, 63x images of astrocytes or astrocyte clusters from
891 40µm sections were captured on the Leica Stellaris 8 Confocal and loaded into ImageJ. Composite
892 images merging the DAPI channel for all nuclei, Sox9 channel for astrocytic nuclei, and the RFP
893 channel for astrocytes were generated. Using the line tool, a line was manually drawn from the
894 edge of one Sox9+ nucleus within mCherry to the closest Sox9+ nucleus and the length of the line
895 was measured. Each distance between neighbors was recorded from the same animal as technical
896 replicates. Data from biological replicates were analyzed using a nested t-test. To quantify the
897 number of Sox9+ nuclei, the composite images from above were used, and the number of Sox9+
898 nuclei within mCherry signal was manually counted. The number of Sox9+ nuclei per cell or
899 cluster were recorded as technical replicates per mouse. The number of mice and cells/mouse
900 analyzed are specified in the figure legend for each experiment. In the Drp1 conditional deletion
901 mouse model, V1 cortical images of 30µm sections were taken on the Leica Stellaris 8 Confocal
902 at 20x with 0.75 optical zoom. Single optical section images were loaded onto Imaris with a z-size
903 of 0.01 µm. Selecting the tdTomato channel, soma spots were generated with an estimated XY
904 diameter of 7.5 µm and with background subtraction using Imaris Spots tool. Object-Object
905 statistics were collected for the spots generated. Once these soma spots were generated, distance
906 to nearest neighbor and average distance to 9 neighbors were analyzed. Data from biological
907 replicates were analyzed using a nested t-test and Kolmogorov-Smirnov test. The number of mice
908 and cells/mouse analyzed are specified in the figure legend for each experiment.

909 *Connexin43 volume analysis* To quantify the amount of Connexin43 within astrocytes in the sparse
910 Drp1 knockdown PALE model, 93x images (0.5 µm z-step, 10 µm z-stacks) from 40µm sections
911 of astrocytes or clusters were taken on the Leica Stellaris 8 Confocal. Criteria for inclusion required
912 the astrocyte to be located within layer 2/3, 4, and 5 of the visual cortex, express the fluorescent
913 label, and have at least 10µm in the z-dimension contained within the section. For each astrocyte
914 or astrocyte cluster, the Imaris surface tool was used to render the astrocyte volume. This astrocyte
915 volume was then used to mask the Cx43 channel, and then Imaris surface tool was used to generate
916 surface volumes of Cx43 puncta within the astrocyte volume territory only. Data from biological
917 replicates were analyzed using a nested t-test. The number of mice and cells/mouse analyzed are
918 specified in the figure legend for each experiment.

919 *Astrocyte density analysis* For quantifying the density of astrocytes in the Drp1 conditional
920 deletion model, V1 cortical images of 30µm sections were taken on the Leica Stellaris 8 Confocal
921 at 20x with 0.75 optical zoom. Using the tdTomato channel on ImageJ, a rectangular region of
922 interest (ROI) that encompassed all cortical layers of the visual cortex was selected and saved to
923 the ROI manager in ImageJ. Within the multi-layer rectangular ROI, ROIs for each cortical layer
924 were drawn and saved. The area of each ROI was recorded. These imaging parameters and ROIs
925 were also used for the *Cortical Astrocyte coverage analysis* and *Drp1 protein expression analyses*
926 *by immunohistochemistry* below. The 'Show-all' feature on the ROI manager was selected, so that
927 the boundaries between cortical layers were shown. Using the Cell Counter plug-in, tdTomato+
928 somas were manually counted. The number of somas across the cortex was calculated as the sum
929 of tdTomato+ somas in all cortical layers. Density of tdTomato+ somas was calculated by dividing
930 the number of tdTomato+ somas by their corresponding ROI area. GFAP+ cell density was
931 calculated and analyzed in the same manner, using the GFAP channel instead of the tdTomato
932 channel. Three sections were analyzed as technical replicates per mouse. Data from biological
933 replicates were analyzed using a two-way ANOVA with Sidak's multiple comparisons test. The
934 number of mice and cells/mouse analyzed are specified in the figure legend for each experiment.

935 *Cortical Astrocyte coverage analysis* To quantify astrocyte coverage across the cortex in the Drp1
936 conditional deletion model, cortical images were captured and divided into multiple ROIs for
937 analysis as described above in *Astrocyte density analysis*. Using the threshold tool in ImageJ, the
938 tdTomato channel coverage was binarized and saved as a tdTomato mask. Then, selecting each
939 cortical ROI, the area of tdTomato coverage from the mask generated across the cortex and per
940 layer was collected. tdTomato coverage was defined as the percent of tdTomato+ area divided by
941 the density of tdTomato+ cells. GFAP coverage was calculated and analyzed in the same manner,
942 using the GFAP channel instead of the tdTomato channel. GFAP coverage likewise normalized by
943 tdTomato density. Three sections were analyzed as technical replicates per mouse. Data from
944 biological replicates were analyzed using a two-way ANOVA with Sidak's multiple comparisons
945 test. The number of mice and cells/mouse analyzed are specified in the figure legend for each
946 experiment.

947 *Drp1 protein expression analyses by immunohistochemistry* For quantifying Drp1 protein levels
948 in the Drp1 conditional deletion model, cortical images were captured and divided into multiple

949 ROIs for analysis as described above in *Astrocyte density analysis*. Then a mask of the tdTomato
950 channel was applied to the Drp1 channel and mean gray value of Drp1 within astrocytes was
951 collected per layer and across the cortex using ImageJ. The collected values were normalized to
952 tdTomato+ soma density. Three sections were analyzed as technical replicates per mouse. Data
953 from biological replicates were analyzed using a two-way ANOVA with Sidak's multiple
954 comparisons test. The number of mice and cells/mouse analyzed are specified in the figure legend
955 for each experiment.

956 *Cx43 protein expression analysis by immunohistochemistry* To measure Cx43 protein levels in
957 astrocytes in the Drp1 conditional deletion model, cortical images were captured as described
958 above in *Astrocyte density analysis*. ImageJ was used to subtract background from the Cx43
959 channel with a rolling ball radius of 50 units. Following background subtraction, individual
960 astrocytes within layers 2/3, 4, or 5 were outlined with the freehand tool using tdTomato to
961 determine astrocyte territories, and astrocyte outlines were saved as ROIs. Astrocyte ROIs were
962 applied to Cx43 channel and the mean gray value of Cx43 signal was collected per astrocyte and
963 normalized by the ROI area. Three sections were analyzed as technical replicates per mouse. Data
964 from biological replicates were analyzed using a nested t-test, Kolmogorov-Smirnov test. The
965 number of mice and cells/mouse analyzed are specified in the figure legend for each experiment.

966 *Cortical thickness analysis:* To measure cortical thickness in Drp1 cWT and cKO mice, 10x images
967 of V1 cortices were taken on the Leica Stellaris 8 confocal. Images were loaded into ImageJ and
968 the line tool was used to record length. Three lines per section were drawn from the subventricular
969 zone to the Pia. The lengths of these lines were averaged per section for 3 sections per mouse, and
970 data from each section was plotted as a technical replicate per mouse. Data from biological
971 replicates were analyzed using a nested t-test.

972 **Quantification and statistical analysis**

973 All statistical analyses were performed using Graphpad Prism 9. The exact number of replicates,
974 specific statistical tests, and P values for each experiment are indicated in the figures and figure
975 legends. All data are represented as mean ± SEM, and individual data points are shown for all data,
976 where applicable. Where indicated, nested t-tests were applied with an alpha threshold of 0.05 for

977 adjusted P-value. A Geisser-Greenhouse correction was used for both One-way and Two-way
978 ANOVA analyses. All experimental animals that appeared healthy at the time of tissue collection
979 were processed for data collection. Specific details for inclusion, exclusion, and randomization are
980 included in the specific subsections of the Materials and methods details section.

981

ACKNOWLEDGMENTS

We thank Drs. Romain Cartoni and Chantell Evans for critical feedback about the manuscript. We thank Sarah Johnson, Gracie Manigault, and Donna Porter for their excellent technical help. This work was supported by a Paul and Daisy Soros Fellowship (2020) and an HHMI Gilliam Fellowship (GT15076) to MPRS, a Chan Zuckerberg Initiative Neurodegeneration Challenge Network Collaborative grant (DAF2018-191999 and DAF2021-237435) to CE, an N.I.H. grant U19-NS123719 to CE and GY, and by the joint efforts of MJFF and the Aligning Science Across Parkinson's (ASAP) initiative. MJFF administers the grant ASAP-020607 to CE for ASAP and the Michael J Fox Foundation. Dr. Cagla Eroglu is an HHMI Investigator.

IP RIGHTS NOTICE

This article is subject to HHMI's Open Access to Publications policy. HHMI lab heads have previously granted a nonexclusive CC BY 4.0 license to the public and a sublicensable license to HHMI in their research articles. Pursuant to those licenses, the author-accepted manuscript of this article can be made freely available under a CC BY 4.0 license immediately upon publication.

AUTHOR CONTRIBUTIONS

Conceptualization, MPRS and CE; Methodology, MPRS, SK, VR, BL; Investigation, MPRS, SK, VR, GS; Formal analysis, MPR, SK, VR; Resources, MPRS, BL, GY, HS; Writing – original draft, MPRS, SK, CE; Writing – Review & Editing, MPRS, SK, VR, BL, GS, HS, GY, CE; Funding Acquisition, MPRS, GY, and CE.

1002 **REFERENCES**

1003 Abati, E., A. Manini, D. Velardo, R. Del Bo, L. Napoli, F. Rizzo, M. Moggio, N. Bresolin, E. Bellone, M.T.
1004 Bassi, M.G. D'Angelo, G.P. Comi, and S. Corti. 2022. Clinical and genetic features of a cohort
1005 of patients with MFN2-related neuropathy. *Scientific Reports*. 12:6181.
1006 Agarwal, A., P.H. Wu, E.G. Hughes, M. Fukaya, M.A. Tischfield, A.J. Langseth, D. Wirtz, and D.E.
1007 Bergles. 2017. Transient Opening of the Mitochondrial Permeability Transition Pore Induces
1008 Microdomain Calcium Transients in Astrocyte Processes. *Neuron*. 93:587-605.e587.
1009 Allen, N.J., and D.A. Lyons. 2018. Glia as architects of central nervous system formation and
1010 function. *Science*. 362:181-185.
1011 Alvarez, J.I., T. Katayama, and A. Prat. 2013. Glial influence on the blood brain barrier. *Glia*. 61:1939-
1012 1958.
1013 Baldwin, K.T., C.X. Tan, S.T. Strader, C. Jiang, J.T. Savage, X. Elorza-Vidal, X. Contreras, T. Rülicke, S.
1014 Hippenmeyer, R. Estévez, R.R. Ji, and C. Eroglu. 2021. HepaCAM controls astrocyte self-
1015 organization and coupling. *Neuron*. 109:2427-2442.e2410.
1016 Billups, B., and I.D. Forsythe. 2002. Presynaptic Mitochondrial Calcium Sequestration Influences
1017 Transmission at Mammalian Central Synapses. *The Journal of Neuroscience*. 22:5840.
1018 Bushong, E.A., M.E. Martone, and M.H. Ellisman. 2004. Maturation of astrocyte morphology and the
1019 establishment of astrocyte domains during postnatal hippocampal development.
1020 *International Journal of Developmental Neuroscience*. 22:73-86.
1021 Bushong, E.A., M.E. Martone, Y.Z. Jones, and M.H. Ellisman. 2002. Protoplasmic astrocytes in CA1
1022 stratum radiatum occupy separate anatomical domains. *J Neurosci*. 22:183-192.
1023 Casillas-Espinosa, P.M., K.L. Powell, and T.J. O'Brien. 2012. Regulators of synaptic transmission:
1024 roles in the pathogenesis and treatment of epilepsy. *Epilepsia*. 53 Suppl 9:41-58.
1025 Chang, C.-R., and C. Blackstone. 2010. Dynamic regulation of mitochondrial fission through
1026 modification of the dynamin-related protein Drp1. *Annals of the New York Academy of*
1027 *Sciences*. 1201:34.
1028 Chen, F., and J. LoTurco. 2012. A method for stable transgenesis of radial glia lineage in rat neocortex
1029 by piggyBac mediated transposition. *J Neurosci Methods*. 207:172-180.
1030 Chen, H., S.A. Detmer, A.J. Ewald, E.E. Griffin, S.E. Fraser, and D.C. Chan. 2003. Mitofusins Mfn1 and
1031 Mfn2 coordinately regulate mitochondrial fusion and are essential for embryonic
1032 development. *J Cell Biol*. 160:189-200.
1033 Cheung, G., O. Chever, A. Rollenhagen, N. Quenech'du, P. Ezan, J.H.R. Lübke, and N. Rouach. 2023.
1034 Astroglial Connexin 43 Regulates Synaptic Vesicle Release at Hippocampal Synapses. *Cells*.
1035 12.
1036 Chih, B., L. Gollan, and P. Scheiffele. 2006. Alternative splicing controls selective trans-synaptic
1037 interactions of the neuroligin-neurexin complex. *Neuron*. 51:171-178.
1038 Chung, W.S., N.J. Allen, and C. Eroglu. 2015. Astrocytes Control Synapse Formation, Function, and
1039 Elimination. *Cold Spring Harb Perspect Biol*. 7:a020370.
1040 Clasadonte, J., E. Scemes, Z. Wang, D. Boison, and P.G. Haydon. 2017. Connexin 43-Mediated
1041 Astroglial Metabolic Networks Contribute to the Regulation of the Sleep-Wake Cycle.
1042 *Neuron*. 95:1365-1380.e1365.
1043 Clavreul, S., L. Abdeladim, E. Hernández-Garzón, D. Niculescu, J. Durand, S.-H. Ieng, R. Barry, G.
1044 Bonvento, E. Beaurepaire, J. Livet, and K. Loulier. 2019. Cortical astrocytes develop in a
1045 plastic manner at both clonal and cellular levels. *Nature Communications*. 10:4884.

1046 Courchet, J., T.L. Lewis, Jr., S. Lee, V. Courchet, D.Y. Liou, S. Aizawa, and F. Polleux. 2013. Terminal
1047 axon branching is regulated by the LKB1-NUAK1 kinase pathway via presynaptic
1048 mitochondrial capture. *Cell*. 153:1510-1525.
1049 Cunniff, B., A.J. McKenzie, N.H. Heintz, and A.K. Howe. 2016. AMPK activity regulates trafficking of
1050 mitochondria to the leading edge during cell migration and matrix invasion. *Molecular biology*
1051 *of the cell*. 27:2662-2674.
1052 Dermietzel, R., E.L. Hertberg, J.A. Kessler, and D.C. Spray. 1991. Gap junctions between cultured
1053 astrocytes: immunocytochemical, molecular, and electrophysiological analysis. *J Neurosci*.
1054 11:1421-1432.
1055 Fahrner, J.A., R. Liu, M.S. Perry, J. Klein, and D.C. Chan. 2016. A novel de novo dominant negative
1056 mutation in DNM1L impairs mitochondrial fission and presents as childhood epileptic
1057 encephalopathy. *Am J Med Genet A*. 170:2002-2011.
1058 Fiebig, C., S. Keiner, B. Ebert, I. Schäffner, R. Jagasia, D.C. Lie, and R. Beckervordersandforth. 2019.
1059 Mitochondrial Dysfunction in Astrocytes Impairs the Generation of Reactive Astrocytes and
1060 Enhances Neuronal Cell Death in the Cortex Upon Photothrombotic Lesion. *Frontiers in*
1061 *molecular neuroscience*. 12:40-40.
1062 Fonseca, T.B., Á. Sánchez-Guerrero, I. Milosevic, and N. Raimundo. 2019. Mitochondrial fission
1063 requires DRP1 but not dynamins. *Nature*. 570:E34-E42.
1064 Fransson, Å., A. Ruusala, and P. Aspenström. 2006. The atypical Rho GTPases Miro-1 and Miro-2 have
1065 essential roles in mitochondrial trafficking. *Biochemical and biophysical research*
1066 *communications*. 344:500-510.
1067 Friedman, J.R., and J. Nunnari. 2014. Mitochondrial form and function. *Nature*. 505:335-343.
1068 Giaume, C., A. Koulakoff, L. Roux, D. Holcman, and N. Rouach. 2010. Astroglial networks: a step
1069 further in neuroglial and gliovascular interactions. *Nat Rev Neurosci*. 11:87-99.
1070 Gollihue, J.L., and C.M. Norris. 2020. Astrocyte mitochondria: Central players and potential
1071 therapeutic targets for neurodegenerative diseases and injury. *Ageing Res Rev*. 59:101039.
1072 Göbel, J., P. Pelzer, E. Engelhardt, V. Sakthivelu, H.M. Jahn, M. Jevtic, K. Folz-Donahue, C. Kukat, A.
1073 Schauss, C.K. Frese, A. Ghanem, K.-K. Conzelmann, E. Motori, and M. Bergami. 2019.
1074 Mitochondrial fusion in reactive astrocytes coordinates local metabolic domains to promote
1075 vascular repair. *bioRxiv*:657999.
1076 Haseleu, J., E. Anlauf, S. Blaess, E. Endl, and A. Derouiche. 2013. Studying subcellular detail in fixed
1077 astrocytes: dissociation of morphologically intact glial cells (DIMIGs). *Frontiers in Cellular*
1078 *Neuroscience*. 7.
1079 Holt, L.M., R.D. Hernandez, N.L. Pacheco, B. Torres Ceja, M. Hossain, and M.L. Olsen. 2019.
1080 Astrocyte morphogenesis is dependent on BDNF signaling via astrocytic TrkB.T1. *Elife*. 8.
1081 Hösli, L., N. Binini, K.D. Ferrari, L. Thieren, Z.J. Looser, M. Zuend, H.S. Zanker, S. Berry, M. Holub, W.
1082 Möbius, T. Ruhwedel, K.A. Nave, C. Giaume, B. Weber, and A.S. Saab. 2022. Decoupling
1083 astrocytes in adult mice impairs synaptic plasticity and spatial learning. *Cell Rep*. 38:110484.
1084 Ignatenko, O., D. Chilov, I. Paetau, E. de Miguel, C.B. Jackson, G. Capin, A. Paetau, M. Terzioglu, L.
1085 Euro, and A. Suomalainen. 2018. Loss of mtDNA activates astrocytes and leads to spongiotic
1086 encephalopathy. *Nature Communications*. 9:70.
1087 Kameritsch, P., K. Pogoda, and U. Pohl. 2012. Channel-independent influence of connexin 43 on cell
1088 migration. *Biochim Biophys Acta*. 1818:1993-2001.
1089 Ke, P., J. Gu, J. Liu, Y. Liu, X. Tian, Y. Ma, Y. Meng, and F. Xiao. 2023. Syntabulin regulates neuronal
1090 excitation/inhibition balance and epileptic seizures by transporting syntaxin 1B. *Cell Death*
1091 *Discov*. 9:187.

1092 König, T., H. Nolte, M.J. Aaltonen, T. Tatsuta, M. Krols, T. Stroh, T. Langer, and H.M. McBride. 2021.
1093 MIROs and DRP1 drive mitochondrial-derived vesicle biogenesis and promote quality
1094 control. *Nat Cell Biol*. 23:1271-1286.
1095 Lagos-Cabré, R., F. Burgos-Bravo, A.M. Avalos, and L. Leyton. 2019. Connexins in Astrocyte
1096 Migration. *Front Pharmacol*. 10:1546.
1097 Lhuissier, C., B.E. Wagner, A. Vincent, G. Garraux, O. Hougrand, R. Van Coster, V. Benoit, D.
1098 Karadurmus, G. Lenaers, N. Gueguen, A. Chevrollier, and I. Maystadt. 2022. Case report:
1099 Thirty-year progression of an EMPF1 encephalopathy due to defective mitochondrial and
1100 peroxisomal fission caused by a novel de novo heterozygous DNM1L variant. *Front Neurol*.
1101 13:937885.
1102 Li, Z., K. Okamoto, Y. Hayashi, and M. Sheng. 2004. The importance of dendritic mitochondria in the
1103 morphogenesis and plasticity of spines and synapses. *Cell*. 119:873-887.
1104 Liu, X., Z. Zhang, D. Li, M. Lei, Q. Li, and P. Zhang. 2021. DNM1L-Related Mitochondrial Fission
1105 Defects Presenting as Encephalopathy: A Case Report and Literature Review. *Front Pediatr*.
1106 9:626657.
1107 Losón, O.C., Z. Song, H. Chen, and D.C. Chan. 2013. Fis1, Mff, MiD49, and MiD51 mediate Drp1
1108 recruitment in mitochondrial fission. *Molecular biology of the cell*. 24:659-667.
1109 Lovatt, D., U. Sonnewald, H.S. Waagepetersen, A. Schousboe, W. He, J.H.C. Lin, X. Han, T. Takano, S.
1110 Wang, F.J. Sim, S.A. Goldman, and M. Nedergaard. 2007. The Transcriptome and Metabolic
1111 Gene Signature of Protoplasmic Astrocytes in the Adult Murine Cortex. *The Journal of*
1112 *Neuroscience*. 27:12255.
1113 López-Doménech, G., Nathalie F. Higgs, V. Vaccaro, H. Roš, I.L. Arancibia-Cárcamo, Andrew F.
1114 MacAskill, and Josef T. Kittler. 2016. Loss of Dendritic Complexity Precedes
1115 Neurodegeneration in a Mouse Model with Disrupted Mitochondrial Distribution in Mature
1116 Dendrites. *Cell Reports*. 17:317-327.
1117 López-Doménech, G., and J.T. Kittler. 2023. Mitochondrial regulation of local supply of energy in
1118 neurons. *Curr Opin Neurobiol*. 81:102747.
1119 Middeldorp, J., and E.M. Hol. 2011. GFAP in health and disease. *Progress in Neurobiology*. 93:421-
1120 443.
1121 Moffat, J., D.A. Grueneberg, X. Yang, S.Y. Kim, A.M. Kloepfer, G. Hinkle, B. Piqani, T.M. Eisenhaure, B.
1122 Luo, J.K. Grenier, A.E. Carpenter, S.Y. Foo, S.A. Stewart, B.R. Stockwell, N. Hacohen, W.C.
1123 Hahn, E.S. Lander, D.M. Sabatini, and D.E. Root. 2006. A lentiviral RNAi library for human and
1124 mouse genes applied to an arrayed viral high-content screen. *Cell*. 124:1283-1298.
1125 Motori, E., J. Puyal, N. Toni, A. Ghanem, C. Angeloni, M. Malaguti, G. Cantelli-Forti, B. Berninger, K.-
1126 K. Conzelmann, M. Götz, Konstanze F. Winklhofer, S. Hrelia, and M. Bergami. 2013.
1127 Inflammation-Induced Alteration of Astrocyte Mitochondrial Dynamics Requires Autophagy
1128 for Mitochondrial Network Maintenance. *Cell Metabolism*. 18:844-859.
1129 Ni, H.M., J.A. Williams, and W.X. Ding. 2015. Mitochondrial dynamics and mitochondrial quality
1130 control. *Redox Biol*. 4:6-13.
1131 Oberheim, N.A., G.F. Tian, X. Han, W. Peng, T. Takano, B. Ransom, and M. Nedergaard. 2008. Loss of
1132 astrocytic domain organization in the epileptic brain. *J Neurosci*. 28:3264-3276.
1133 Pellerin, L., and P.J. Magistretti. 1994. Glutamate uptake into astrocytes stimulates aerobic
1134 glycolysis: a mechanism coupling neuronal activity to glucose utilization. *Proc Natl Acad Sci*
1135 *U S A*. 91:10625-10629.
1136 Pellerin, L., G. Pellegri, P.G. Bittar, Y. Charnay, C. Bouras, J.L. Martin, N. Stella, and P.J. Magistretti.
1137 1998. Evidence supporting the existence of an activity-dependent astrocyte-neuron lactate
1138 shuttle. *Dev Neurosci*. 20:291-299.

Popov, A., N. Brazhe, K. Morozova, K. Yashin, M. Bychkov, O. Nosova, O. Sutyagina, A. Brazhe, E. Parshina, L. Li, I. Medyanik, D.E. Korzhevskii, Z. Shenkarev, E. Lyukmanova, A. Verkhratsky, and A. Semyanov. 2023. Mitochondrial malfunction and atrophy of astrocytes in the aged human cerebral cortex. *Nature Communications*. 14:8380.

Rangaraju, V., M. Lauterbach, and E.M. Schuman. 2019. Spatially Stable Mitochondrial Compartments Fuel Local Translation during Plasticity. *Cell*. 176:73-84.e15.

Rash, J.E., T. Yasumura, F.E. Dudek, and J.I. Nagy. 2001. Cell-specific expression of connexins and evidence of restricted gap junctional coupling between glial cells and between neurons. *J Neurosci*. 21:1983-2000.

Ren, D., P. Zheng, J. Feng, Y. Gong, Y. Wang, J. Duan, L. Zhao, J. Deng, H. Chen, S. Zou, T. Hong, and W. Chen. 2020. Overexpression of Astrocytes-Specific GJA1-20k Enhances the Viability and Recovery of the Neurons in a Rat Model of Traumatic Brain Injury. *ACS Chemical Neuroscience*. 11:1643-1650.

Shimura, D., E. Nuebel, R. Baum, S.E. Valdez, S. Xiao, J.S. Warren, J.A. Palatinus, T. Hong, J. Rutter, and R.M. Shaw. 2021. Protective mitochondrial fission induced by stress-responsive protein GJA1-20k. *Elife*. 10.

Smirnova, E., L. Griparic, D.L. Shurland, and A.M. van der Bliek. 2001. Dynamin-related protein Drp1 is required for mitochondrial division in mammalian cells. *Mol Biol Cell*. 12:2245-2256.

Smith, G.M., and G. Gallo. 2018. The role of mitochondria in axon development and regeneration. *Developmental neurobiology*. 78:221-237.

Smyth, J.W., and R.M. Shaw. 2013. Autoregulation of connexin43 gap junction formation by internally translated isoforms. *Cell Rep*. 5:611-618.

Srinivasan, R., T.Y. Lu, H. Chai, J. Xu, B.S. Huang, P. Golshani, G. Coppola, and B.S. Khakh. 2016. New Transgenic Mouse Lines for Selectively Targeting Astrocytes and Studying Calcium Signals in Astrocyte Processes In Situ and In Vivo. *Neuron*. 92:1181-1195.

Steketee, M.B., S.N. Moysidis, J.E. Weinstein, A. Kreymerman, J.P. Silva, S. Iqbal, and J.L. Goldberg. 2012. Mitochondrial dynamics regulate growth cone motility, guidance, and neurite growth rate in perinatal retinal ganglion cells in vitro. *Invest Ophthalmol Vis Sci*. 53:7402-7411.

Stephen, T.L., N.F. Higgs, D.F. Sheehan, S. Al Awabdh, G. Lopez-Domenech, I.L. Arancibia-Carcamo, and J.T. Kittler. 2015. Miro1 Regulates Activity-Driven Positioning of Mitochondria within Astrocytic Processes Apposed to Synapses to Regulate Intracellular Calcium Signaling. *J Neurosci*. 35:15996-16011.

Stogsdill, J.A., J. Ramirez, D. Liu, Y.-H. Kim, K.T. Baldwin, E. Enustun, T. Ejikeme, R.-R. Ji, and C. Eroglu. 2017. Astrocytic Neuroligins Control Astrocyte Morphogenesis and Synaptogenesis. *Nature*. 551:192-197.

Supplie, L.M., T. Düking, G. Campbell, F. Diaz, C.T. Moraes, M. Götz, B. Hamprecht, S. Boretius, D. Mahad, and K.-A. Nave. 2017. Respiration-Deficient Astrocytes Survive As Glycolytic Cells In Vivo. *The Journal of Neuroscience*. 37:4231.

Takano, T., J.T. Wallace, K.T. Baldwin, A.M. Purkey, A. Uezu, J.L. Courtland, E.J. Soderblom, T. Shimogori, P.F. Maness, C. Eroglu, and S.H. Soderling. 2020. Chemico-genetic discovery of astrocytic control of inhibition in vivo. *Nature*. 588:296-302.

Tan, C.X., D.S. Bindu, E.J. Hardin, K. Sakers, R. Baumert, J.J. Ramirez, J.T. Savage, and C. Eroglu. 2023. δ-Catenin controls astrocyte morphogenesis via layer-specific astrocyte-neuron cadherin interactions. *J Cell Biol*. 222.

Uo, T., J. Dworzak, C. Kinoshita, D.M. Inman, Y. Kinoshita, P.J. Horner, and R.S. Morrison. 2009. Drp1 levels constitutively regulate mitochondrial dynamics and cell survival in cortical neurons. *Exp Neurol*. 218:274-285.

Vanstone, J.R., A.M. Smith, S. McBride, T. Naas, M. Holcik, G. Antoun, M.-E. Harper, J. Michaud, E. Sell, P. Chakraborty, M. Tetreault, J. Majewski, S. Baird, K.M. Boycott, D.A. Dyment, A. MacKenzie, M.A. Lines, and C. Care4Rare. 2016. DNM1L-related mitochondrial fission defect presenting as refractory epilepsy. *European Journal of Human Genetics*. 24:1084-1088.

Wakabayashi, J., Z. Zhang, N. Wakabayashi, Y. Tamura, M. Fukaya, T.W. Kensler, M. Iijima, and H. Sesaki. 2009a. The dynamin-related GTPase Drp1 is required for embryonic and brain development in mice. *J Cell Biol*. 186:805-816.

Wakabayashi, J., Z. Zhang, N. Wakabayashi, Y. Tamura, M. Fukaya, T.W. Kensler, M. Iijima, and H. Sesaki. 2009b. The dynamin-related GTPase Drp1 is required for embryonic and brain development in mice. *The Journal of cell biology*. 186:805-816.

Wang, Y., C. Wang, P. Ranefall, G.J. Broussard, G. Shi, B. Lyu, C.T. Wu, L. Tian, and G. Yu. 2020. SynQuant: an automatic tool to quantify synapses from microscopy images. *Bioinformatics*. 36:1599-1606.

Wiencken-Barger, A.E., B. Djukic, K.B. Casper, and K.D. McCarthy. 2007. A role for Connexin43 during neurodevelopment. *Glia*. 55:675-686.

Xiao, S., D. Shimura, R. Baum, D.M. Hernandez, S. Agvanian, Y. Nagaoka, M. Katsumata, P.D. Lampe, A.G. Kleber, T. Hong, and R.M. Shaw. 2020. Auxiliary trafficking subunit GJA1-20k protects connexin-43 from degradation and limits ventricular arrhythmias. *The Journal of Clinical Investigation*. 130:4858-4870.

Youle, R.J., and A.M. van der Bliek. 2012. Mitochondrial fission, fusion, and stress. *Science*. 337:1062-1065.

Zehnder, T., F. Petrelli, J. Romanos, E.C. De Oliveira Figueiredo, T.L. Lewis, Jr., N. Déglon, F. Polleux, M. Santello, and P. Bezzi. 2021. Mitochondrial biogenesis in developing astrocytes regulates astrocyte maturation and synapse formation. *Cell Rep*. 35:108952.

Zipursky, S., J. Lee, A. Sergeeva, G. Ahlsen, S. Mannepalli, F. Bahna, K. Goodman, B. Khakh, J. Weiner, L. Shapiro, and B. Honig. 2024. Astrocyte morphogenesis requires self-recognition. *Res Sq*.

Fig 1: Mitochondria increase in number and decrease in size during cortical astrocyte morphogenesis *in vivo.*

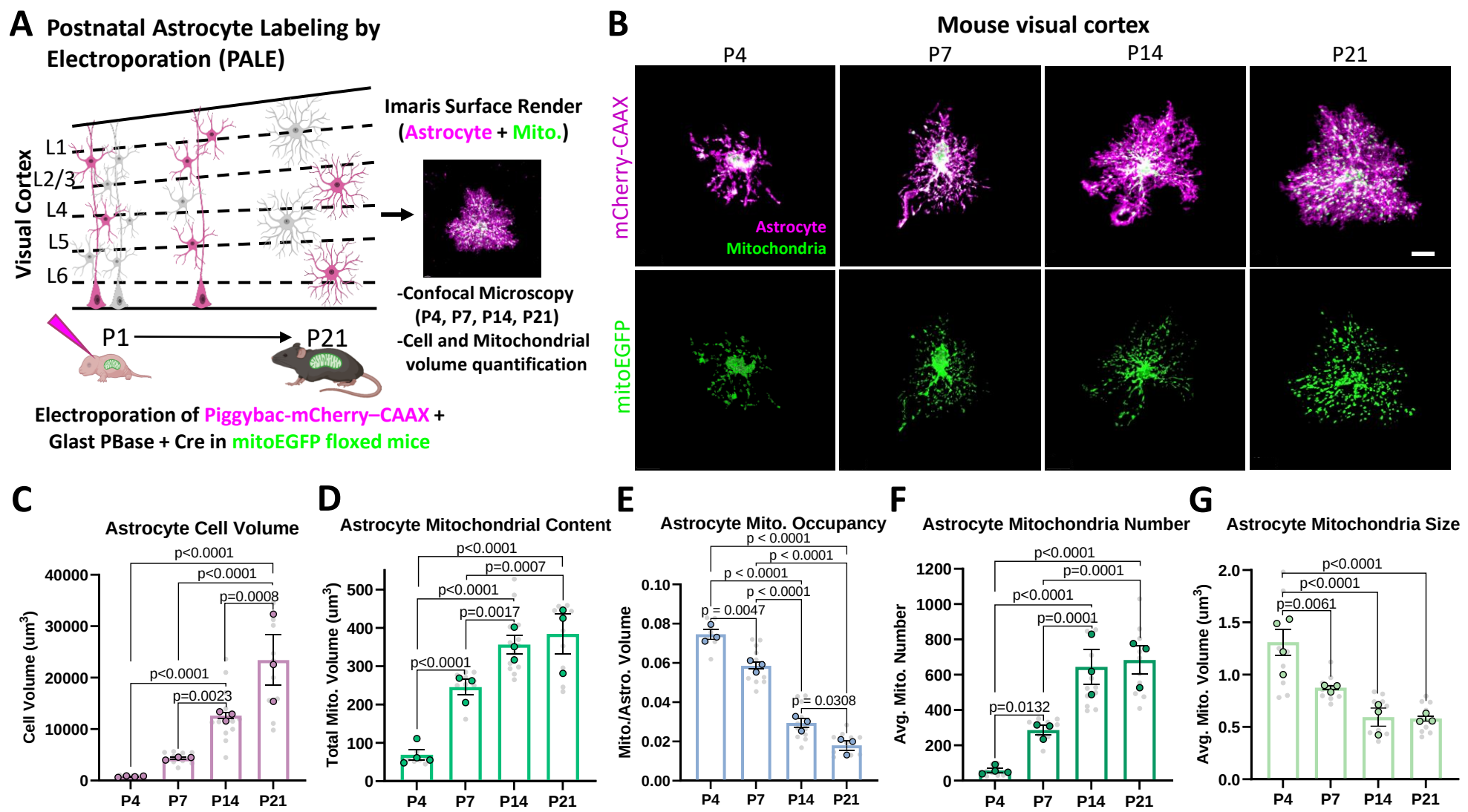

Fig 2: Mitochondrial occupy fine astrocyte processes concurrently with astrocyte morphological arborization *in vitro.*

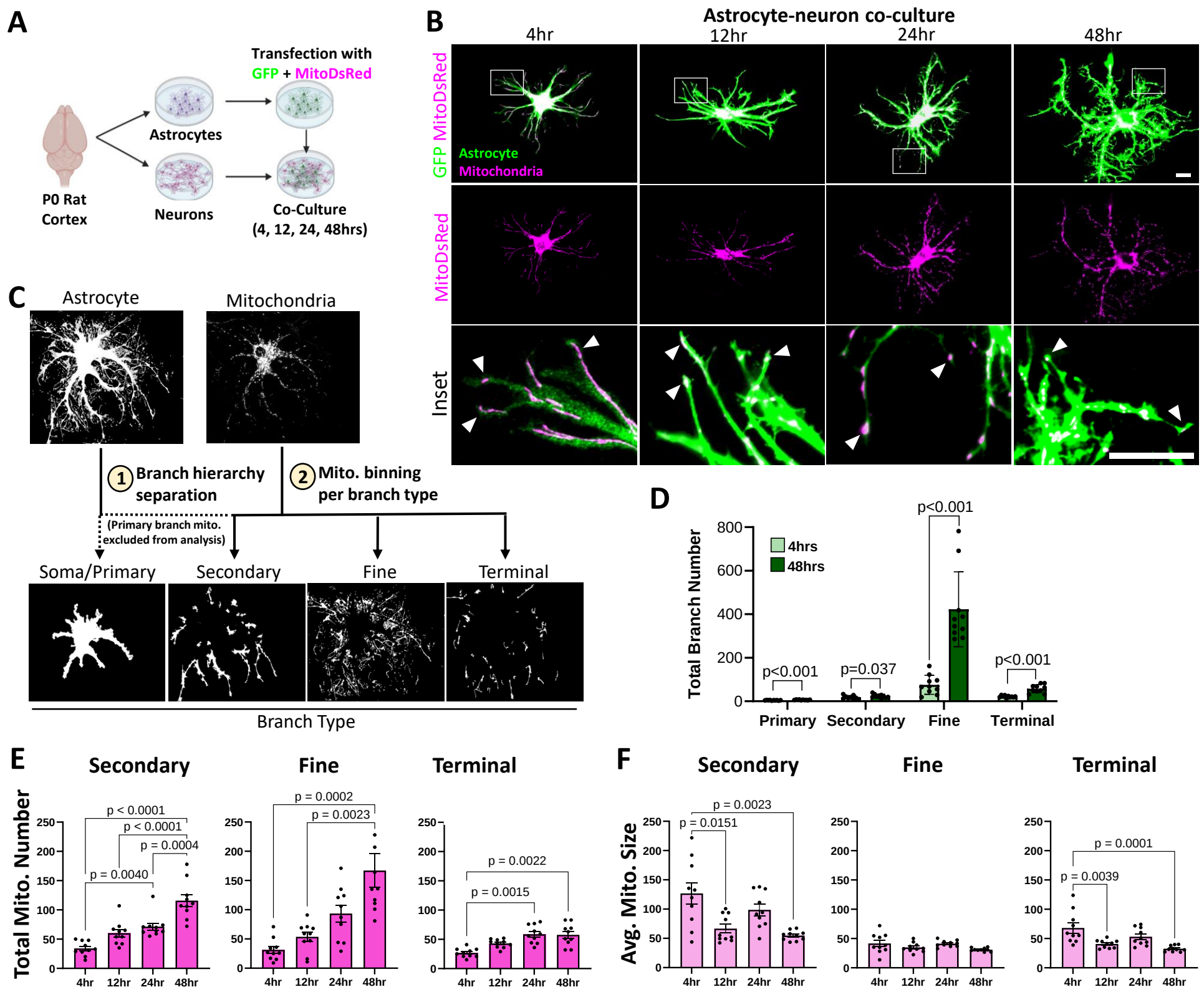

Fig 3: Drp1-induced mitochondrial fission is required for fine astrocyte process formation and mitochondrial localization *in vitro.*

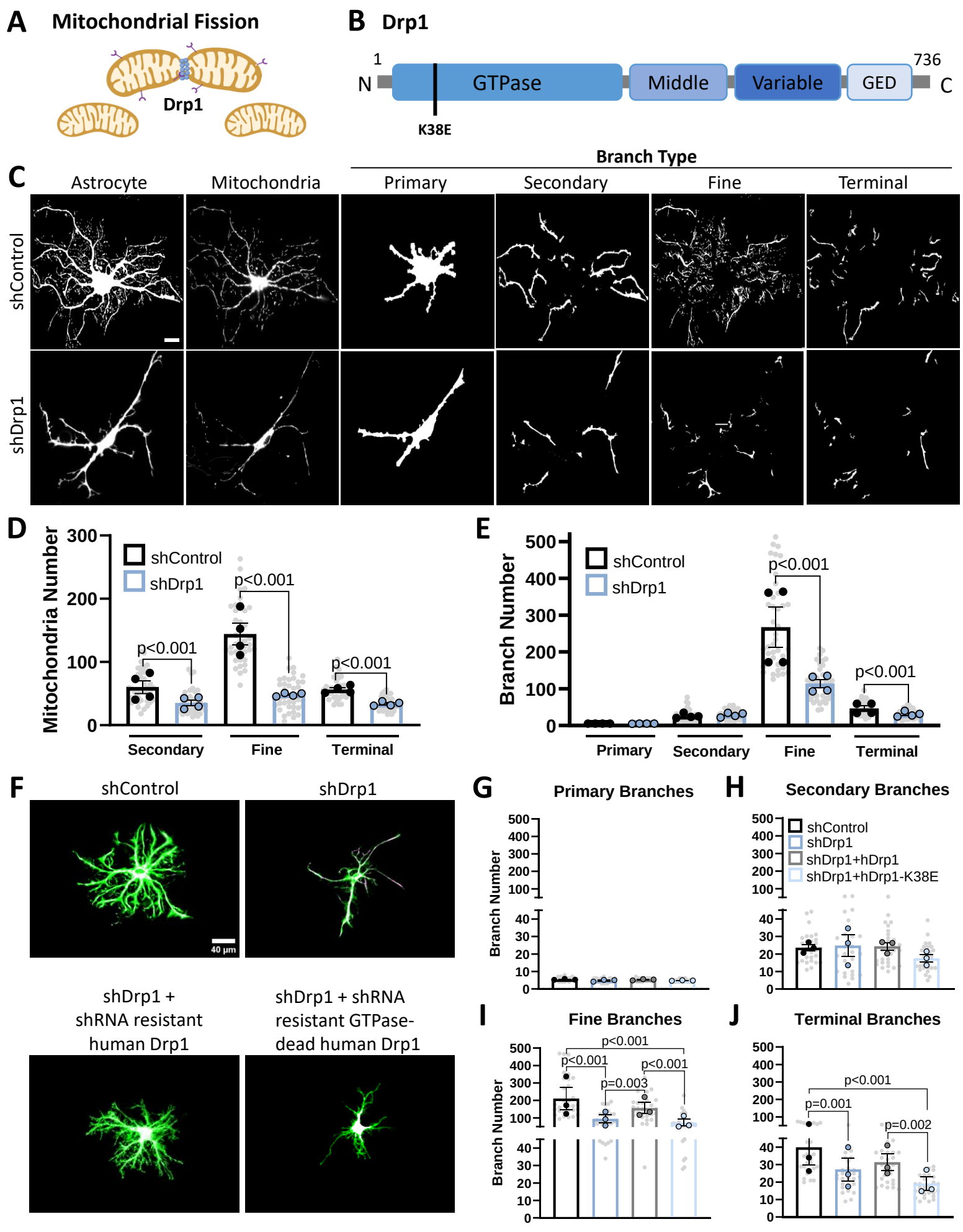

Supplemental 1: Validation of shRNA tools

A

shDrp1	ms	CTATAATGCATGCACTATTTA
	rat	CTATAATGCATGCACTATTTA
	Hm	XXXXAATGCATGCACTATXXX

C

shMiro1	ms	TGGACTGTGCTTCGACGATTT
shMfn1	ms	GCAAGATTACAGGAGTTTCAA

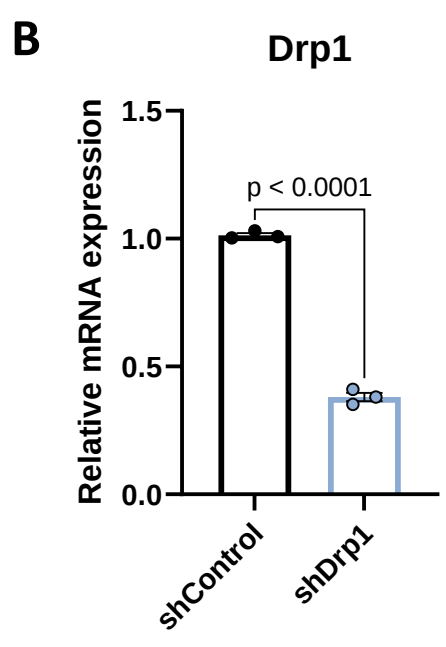

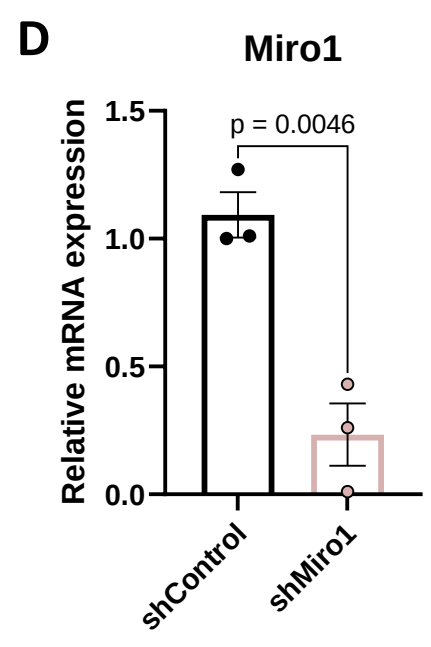

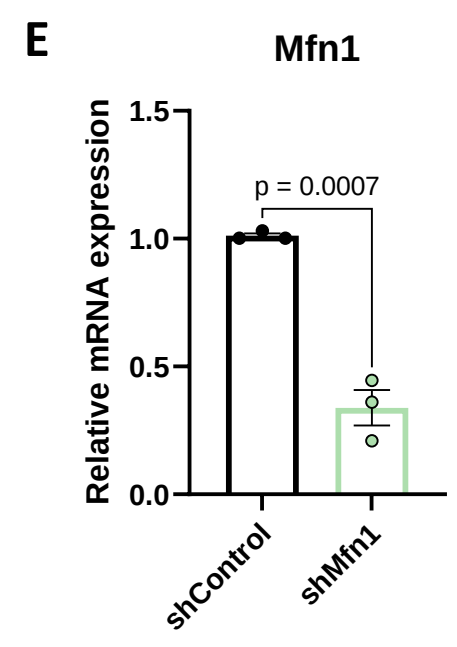

Fig 4: Mitochondrial fission, not fusion nor transport, is required for distal astrocyte process morphogenesis *in vivo*

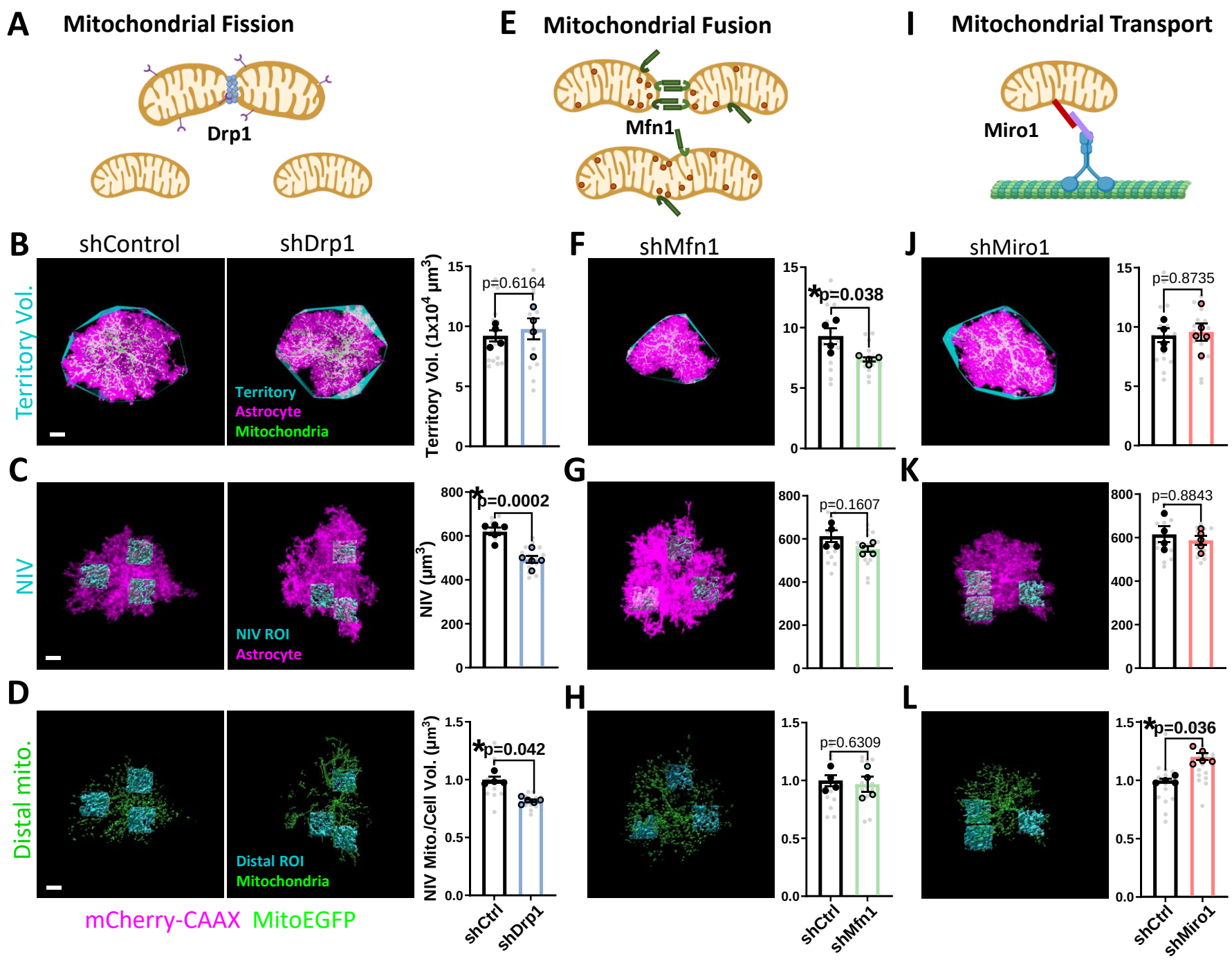

Supplemental 2: Mitochondrial dynamics do not affect astrocyte total mitochondrial content.

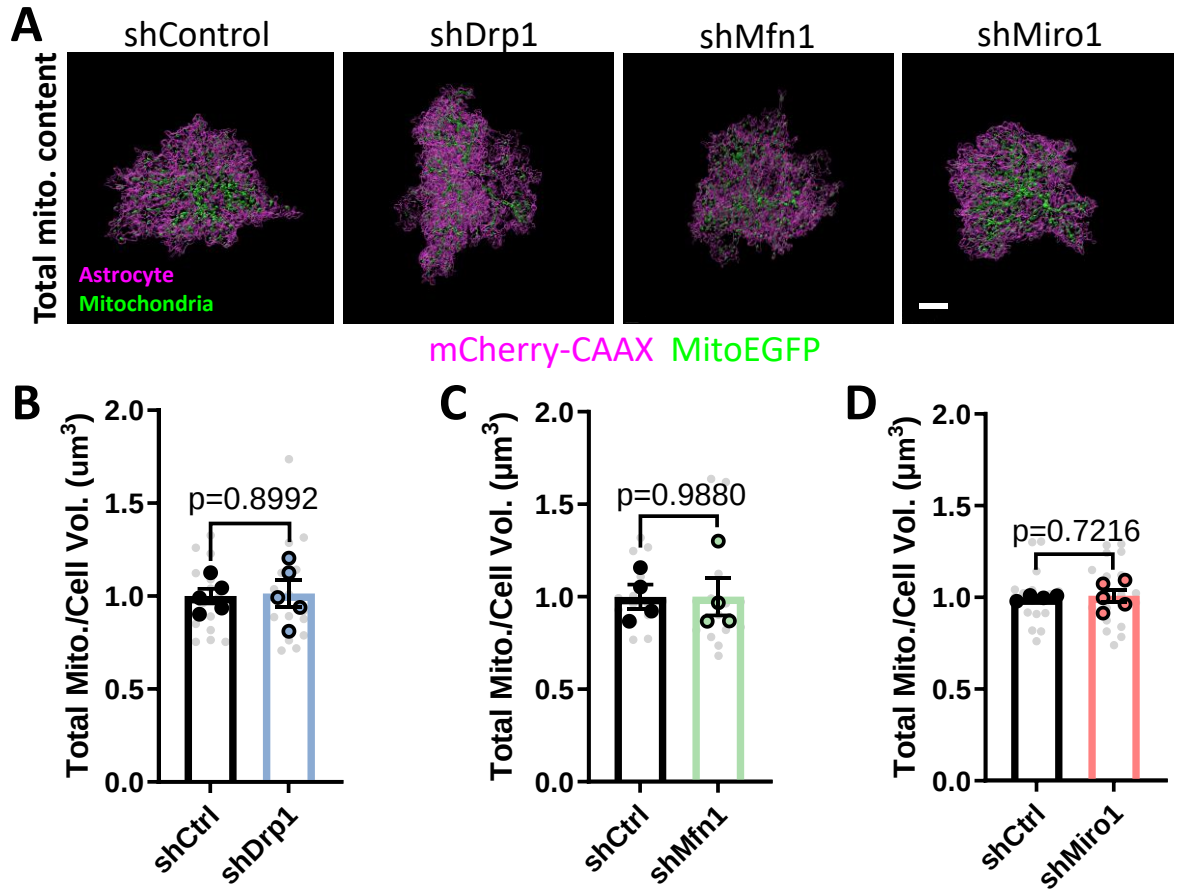

Fig 5: Drp1 controls cortical astrocyte organization during postnatal development

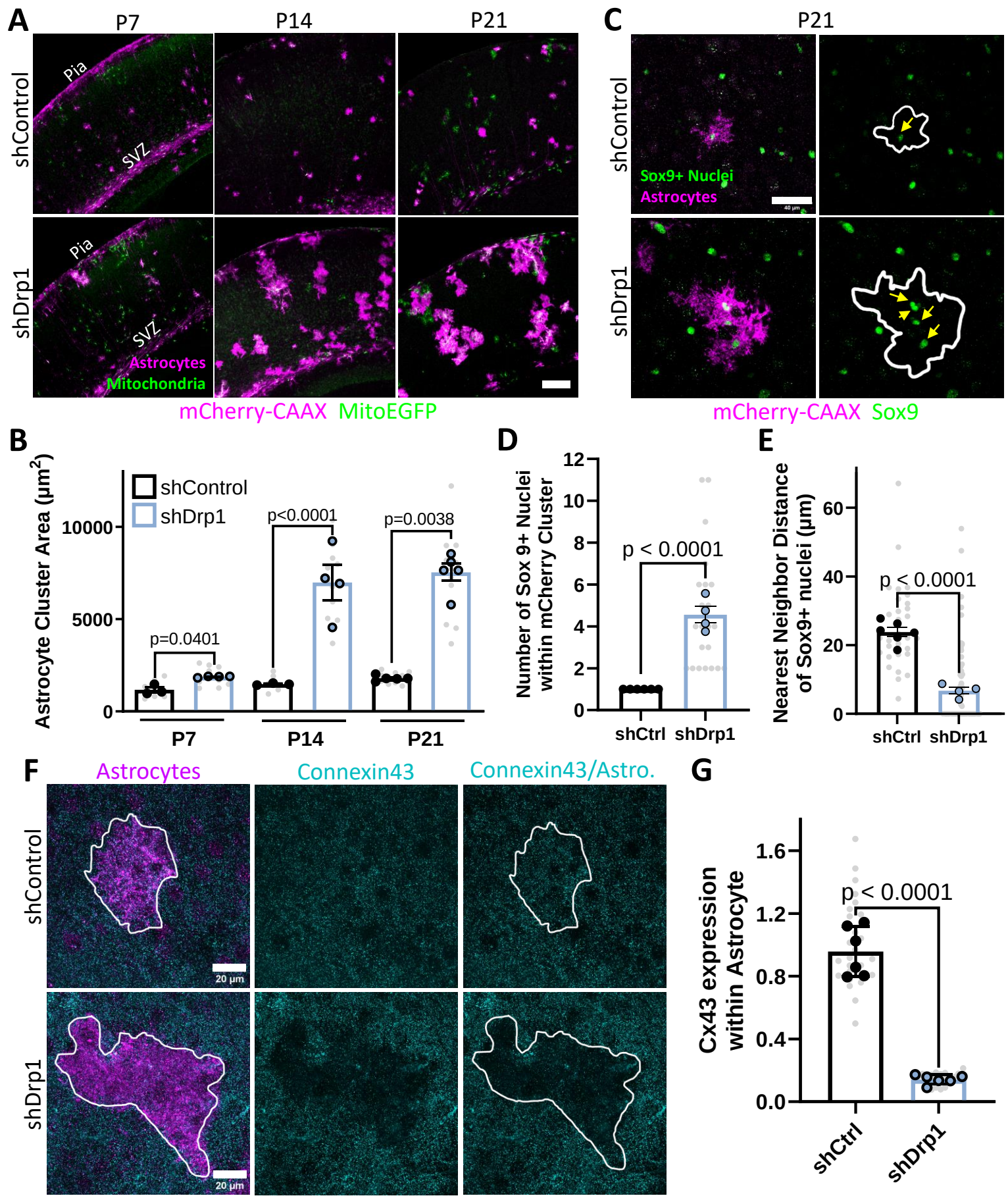

Supplemental 3: shDrp1-induced astrocyte clustering is not a result of increased astrocyte proliferation and is maintained through adulthood

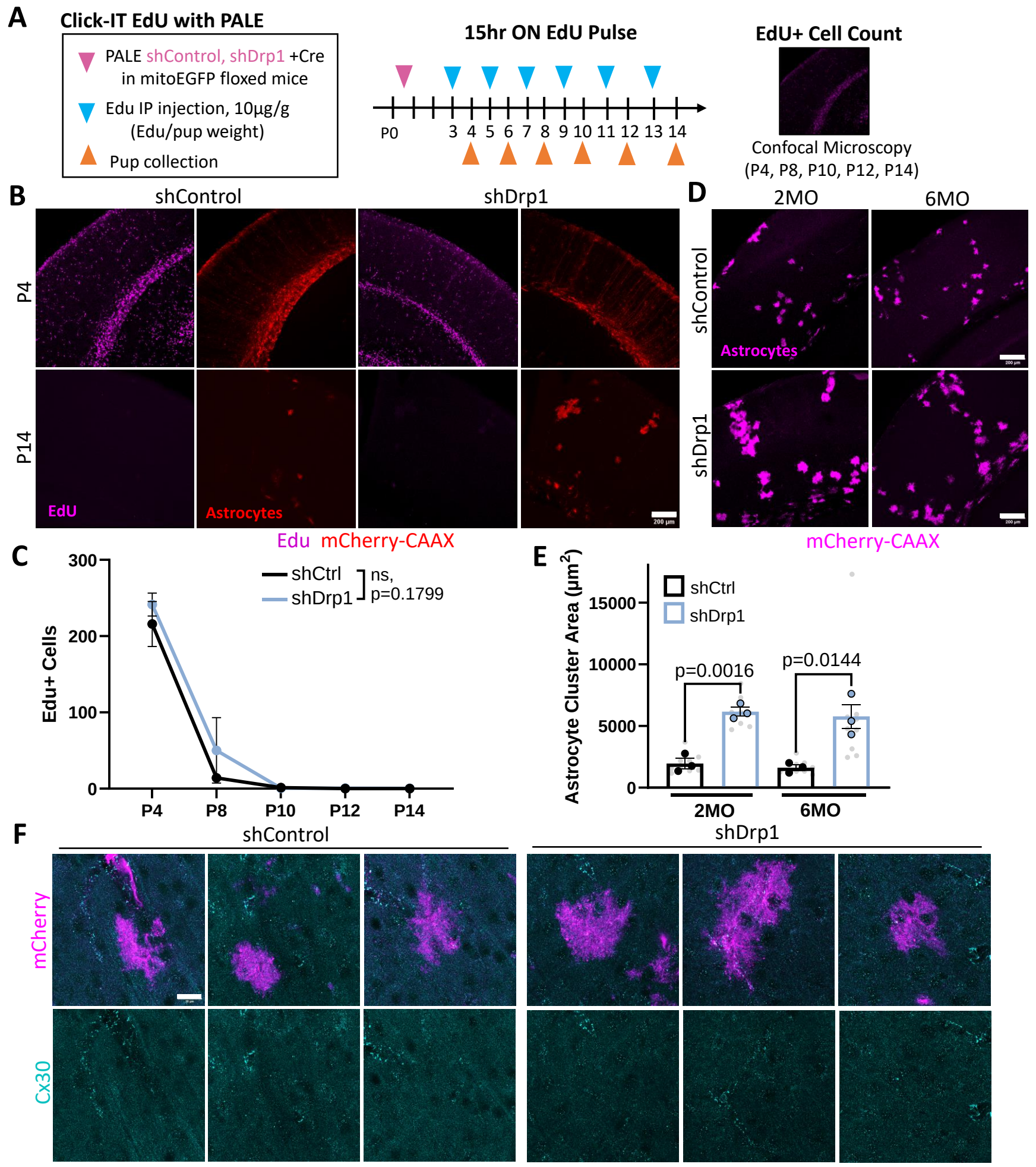

Fig 6: Astrocyte-specific Drp1 cKO induces cortical astrocyte reactivity

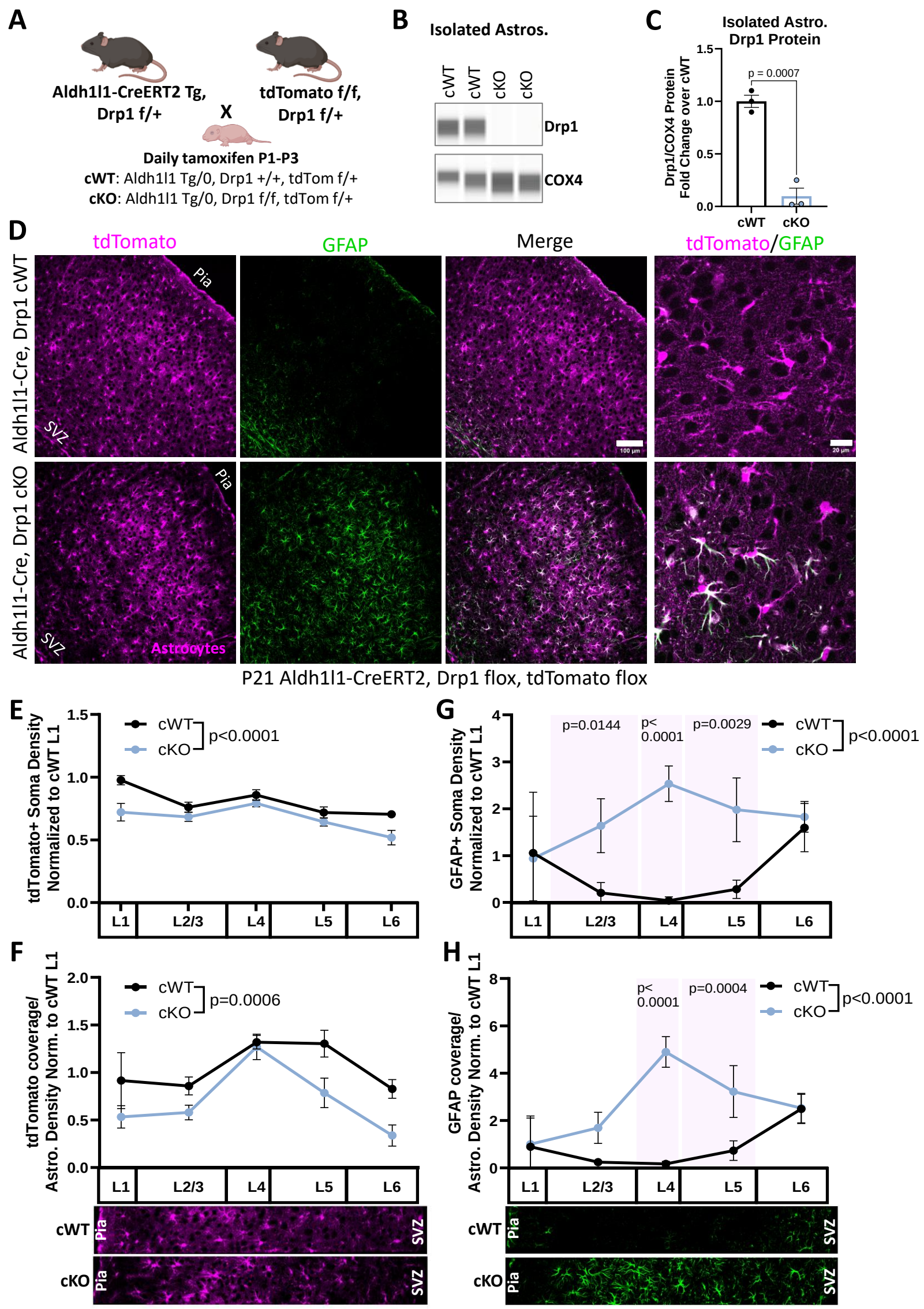

Supplemental 4: Astrocyte-Specific Drp1 cKO mouse characterization

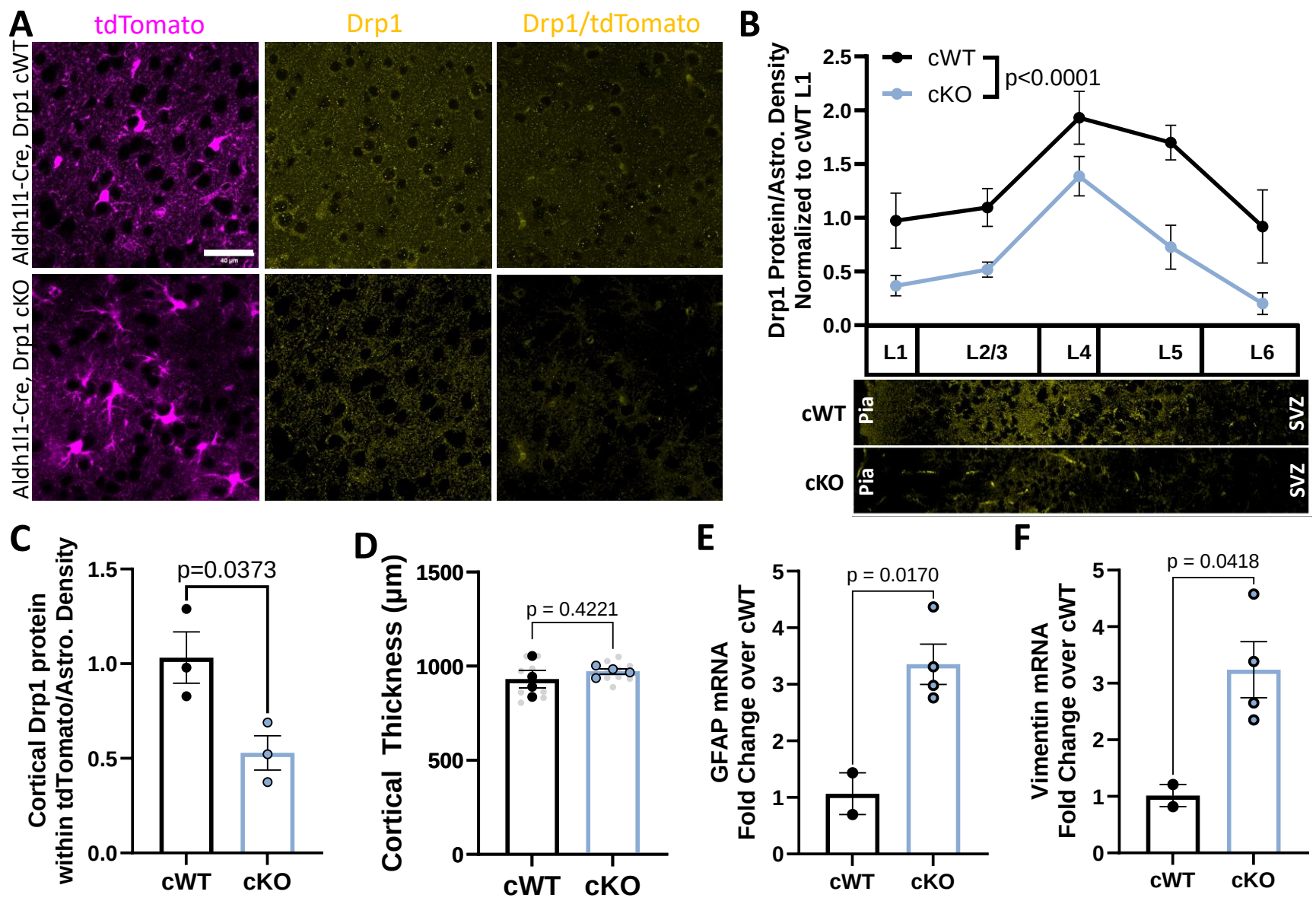
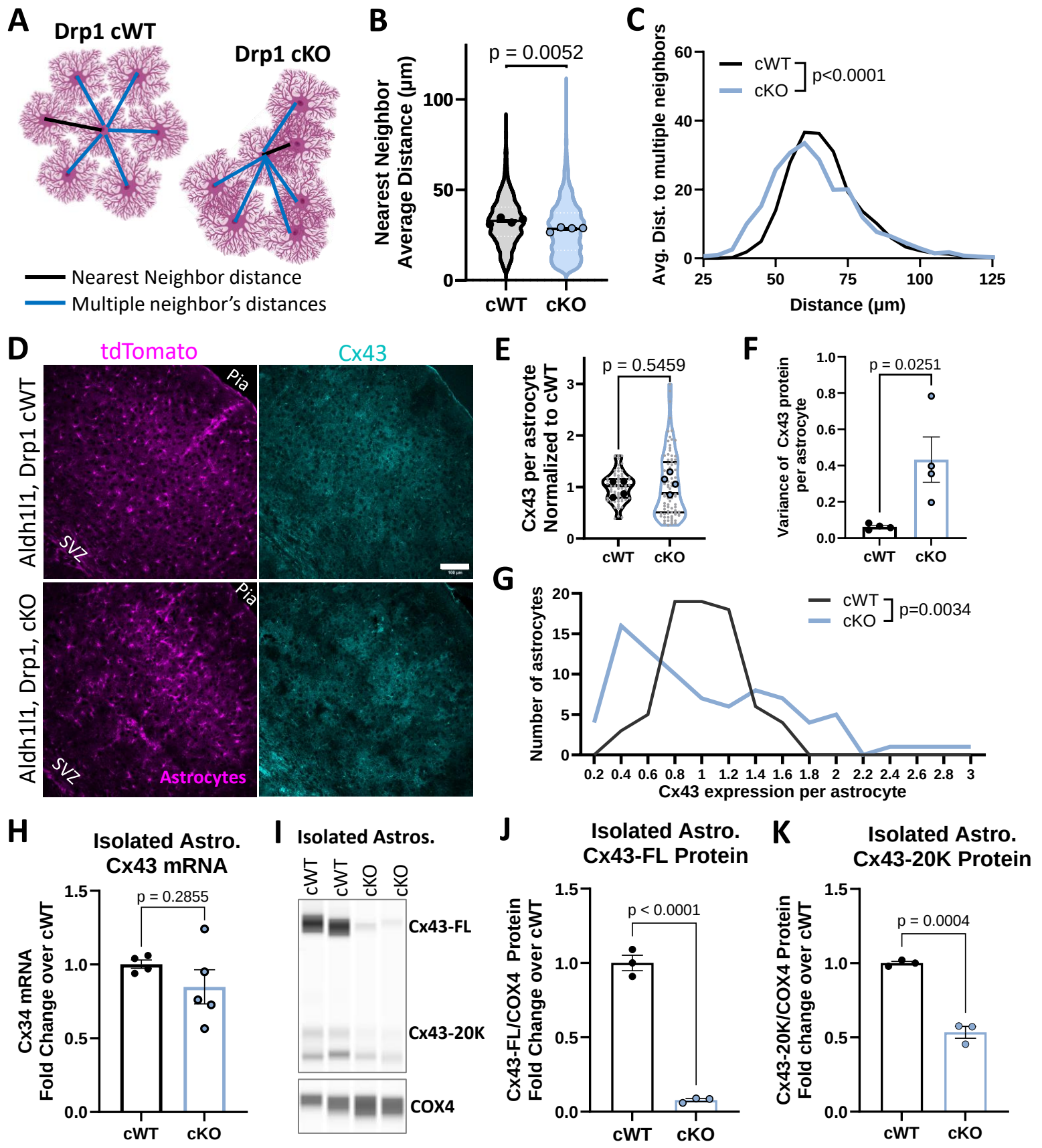
Fig 7: Astrocytic Drp1 loss dysregulates astrocyte organization and Connexin 43 expression in the mouse cortex